UNIVERSIDADE D
COIMBRA

João Pedro Figueiredo de Sá Sousa de Almeida

CARACTERIZAÇÃO E MODELAÇÃO DE UM CONJUNTO QUEIMADOR-PERMUTADOR DE CALOR PARA UTILIZAÇÃO COMO EVAPORADOR EM CICLOS ORGÂNICOS DE RANKINE DE BAIXA POTÊNCIA

VOLUME 1

Dissertação no âmbito do Mestrado Integrado em Engenharia Mecânica, na especialidade de Energia e Ambiente orientada pelo Professor Doutor José Manuel Baranda Moreira da Silva Ribeiro e Mestre João Pedro da Silva Pereira e apresentada ao Departamento de Engenharia Mecânica da Faculdade de Ciências e Tecnologia da Universidade de Coimbra

Setembro de 2019

1 2 9 0

FACULDADE DE CIÊNCIAS E TECNOLOGIA
UNIVERSIDADE D COIMBRA

Characterization and Modelling of a Burner-Heat Exchanger Assembly to be used as an Evaporator in Low Power Organic Rankine Cycles

Submitted in Partial Fulfilment of the Requirements for the Degree of Master in Mechanical Engineering in the speciality of Energy and Environment

Author

João Pedro Figueiredo de Sá Sousa de Almeida

Advisors

Professor José Manuel Baranda Moreira da Silva Ribeiro

Master Eng. João Pedro da Silva Pereira

Jury

President	Professor **Adélio Manuel Rodrigues Gaspar** **Auxiliary Professor at the University of Coimbra**
Vowel	Professor **José Joaquim da Costa** **Auxiliary Professor at the University of Coimbra**
Advisor	Professor **José Manuel Baranda Moreira da Silva Ribeiro** **Auxiliary Professor at the University of Coimbra**

Coimbra, September, 2019

ACKNOWLEDGEMENTS

The development of this entire thesis work was only made possible thanks to the contribution of a number of people who deserve my deepest appreciation.

I would like to thank main advisor, Professor José Manuel Baranda Ribeiro, for giving me the opportunity to work on this area as well as all the support provided and availability shown during the elaboration of this dissertation. Thank you for the comprehensiveness shown in terms of the effort required to complete such type of tasks as I felt that an adequate amount of work was expected from me given my abilities and the nature of the work itself.

I could not also fail to thank M. Eng João Pedro Pereira for all the guidance given during this period as all the work I developed was closely and carefully followed by him. Having João as an advisor clearly enabled me to perform the required tasks with much greater speed and efficiency than I would have done otherwise thanks to all the time he spent working alongside me.

I would also like to express an enormous gratitude towards my parents and grandparents, not only for unconditionally supporting me throughout my whole academic life but also for always expecting the best from me without ever making me feel pressured.

Last but not least, I would like to thank my close friends. Thanks to my Mechanical Engineering fellow mates for making my daily student life so much more enjoyable and for helping whenever needed. A huge thank you to my high-school friends VL^{TM} for providing some much-needed rests and breaks from my work as a student with all the parties/dinners/nights out we experienced together. I could also not fail to mention my childhood friends who grew up with me and never failed to show up to whatever we would arrange, even after all these years. Overall, thank you for making these 5 years at the University of Coimbra so much more enjoyable than they would have been otherwise

Abstract

Micro-CHP has been proving itself as an interesting alternative to traditional energy conversion processes due to its potentials in terms of energy savings and reduction in emissions. This is especially relevant in modern times, when there has been an ever-growing concern about environmental protection. Organic Rankine Cycles (ORCs) are believed to play a large roll in this field due to their vast range of applications, including the possibility of satisfying thermal demands on a domestic level with the added benefit of producing electrical energy in the process.

The goal of the work presented in this dissertation is the construction of a mathematical model capable of simulating the behavior of a Burner and Heat Exchanger assembly to be integrated in an ORC as a direct evaporator.

The model intends to simulate the combustion and heat transfer phenomena between the flue gases and the two fluids used: the working/organic fluid (WF) and liquid water whose intention is to protect the WF from high temperatures (and eventual thermal degradation), thus solving the main problem associated with direct evaporation.

In a final stage the model was compared to experimental data in order to perform its validation. The first step involved the comparison of the model's results to those obtained in a series of preliminary tests where water was used instead of an organic fluid. Without any calibration factor, the overall results concerning the heat transfer in the evaporator only deviated from the tests by little over 5%. After performing the final tests and comparing outputs, it was concluded that the model is capable of describing the overall behavior of these components even if with smaller accuracy (errors up to 10% with no calibration factor). This discrepancy was due to a series of factors such as simplifications in the model, measurement inaccuracies and a few different phenomena which were not accounted for.

Regardless of said inaccuracies, the elaborated model provides useful insight into the way these components behave as well as some particular aspects which are not easily evaluated from experimental tests alone.

Keywords ORC, Micro-CHP, Direct Evaporation, Modelling.

Resumo

Em tempos recentes, tem-se vindo a concluir que a Microcogeração é uma alternativa interessante aos processos tradicionais de conversão de energia devido ao seu potencial em termos de poupanças energéticas bem como de redução de emissões poluentes. Tal é particularmente relevante na atualidade, em que se tem vindo a verificar acrescidas preocupações a nível ambiental. Acredita-se que os Ciclos Orgânicos de Rankine (ORCs) possam vir a desempenhar um papel fundamental neste campo devido à sua vasta gama de aplicações, tais como a possibilidade de satisfazer necessidades térmicas a nível residencial com o benefício acrescido de produzirem energia elétrica no processo.

O objetivo do trabalho apresentado nesta dissertação é a construção de um modelo matemático capaz de simular o comportamento de um conjunto Queimador-Permutador de Calor para ser integrado num ORC como evaporador direto.

O modelo tem por objetivo simular uma série de fenómenos de combustão e transferência de calor entre os gases de escape e os dois fluidos utilizados: o fluido orgânico/de trabalho (WF) e água líquida cujo objetivo consiste em proteger o WF de altas temperaturas (e eventual degradação térmica) resolvendo, deste modo, o maior problema tipicamente associado à vaporização direta.

Na fase final o modelo foi comparado com dados experimentais de modo a efetuar a sua validação. O primeiro passo envolveu a comparação dos resultados do modelo com os obtidos numa série de testes preliminares nos quais água foi utilizada em vez de um fluido orgânico. Sem qualquer fator de calibração, os valores da potência térmica transferida no evaporador apenas se desviaram dos testes em pouco mais de 5%. Após completados os testes finais e os resultados novamente comparados, concluiu-se que o modelo é capaz de descrever o comportamento global destes componentes, ainda que com menor precisão (erros até 10%, sem fatores de calibração). Esta discrepância deveu-se a uma série de fatores tais como simplificações no modelo, erros de medição, etc.

Independentemente das referidas imprecisões, o modelo construído fornece conhecimentos importantes acerca do funcionamento destes componentes bem como de alguns aspetos particulares que não são fáceis de avaliar apenas com ensaios experimentais.

Palavras-chave: ORC, Microcogeração, Vaporização Direta, Modelação.

Contents

LIST OF FIGURES ix
LIST OF TABLES xi
LIST OF SYMBOLS AND ACRONYMS/ ABBREVIATIONS xiii
List of Symbols xiii
Acronyms/Abbreviations xvi
1. INTRODUCTION 1
1.1. Motivation and Objectives 1
1.2. State of the Art Review 5
1.3. Dissertation Structure 6
2. COMBUSTION MODEL 8
3. POST-HEATER MODEL 11
4. EVAPORATOR MODEL 19
4.1. Overview and Heat Transfer Calculations 19
4.2. Internal Heat Transfer Coefficient 25
4.3. Final Considerations 27
5. ANALYSIS OF RESULTS 30
5.1. Combustion Model's Results 30
5.2. Extra Calculations 32
5.2.1. Fin Tip Temperature 32
5.2.2. Pressure Drop in the Gas Flow 34
5.2.3. Pressure Drop in the Working Fluid 35
5.3. Post-Heater & Evaporator Model's Results 38
6. EXPERIMENTAL ANALYSIS 45
6.1. Test Rig Description 45
6.2. Experimental Tests 50
7. MODEL VALIDATION 51
7.1. Preliminary Validation 51
7.2. Final Validation 54
8. CONCLUSIONS 59
8.1. Global Conclusions 59
8.2. Recommendations 60
BIBLIOGRAPHY 62
ANNEX A 65
ANNEX B 67
ANNEX C 69

ANNEX D 71
ANNEX E 73

LIST OF FIGURES

Figure 1.1. Scheme of the developed micro-CHP ORC based prototype. Adapted from [5]. 4

Figure 2.1. Excess of air as a function of the NG volumetric consumption. 8

Figure 3.1. 2D view of the burner (B), post-heater (PH) and evaporator (E) assembly with the control volumes defined for both the water and gas flow. 11

Figure 4.1. Isometric view of the evaporator section. The working fluid runs inside the tubes, in the direction of the arrows, while the gas flows on their exterior. 19

Figure 4.2. 2D view of the evaporator section with the discretization of the gas and fluid flow per control volumes. For this scheme, it was considered *Nc* =8 and only the first and last tubes' CVs are shown. 20

Figure 5.1. Combustion gases' mass flow rate as a function of the burner's power output. 30

Figure 5.2. Flame temperature and excess of air as a function of the burner's power output. 31

Figure 5.3. Flame temperature as a function of the excess of air. 31

Figure 5.4. Weight of each type of pressure drop on the organic fluid. 36

Figure 5.5. Continuous and local pressure losses inside the evaporator. 37

Figure 5.6. Combustion Gases' temperature variation. 38

Figure 5.7. Weight of the heat transfer by convection and radiation on each level. 39

Figure 5.8. Internal Heat Transfer coefficient 39

Figure 5.9. Power Transferred per CV. 39

Figure 5.10. Tube's internal temperature. 40

Figure 5.11. Working fluid's temperature. 40

Figure 5.12. Radial temperature distribution for two-phase flow (a) and superheated vapor (b). 43

Figure 5.13. Power distribution between the two components (including losses). 44

Figure 5.14. Efficiency of the Burner, Post-Heater and Evaporator assembly. 44

Figure 6.1. Location of the fluid and water thermocouples on the Evaporator and Post-Heater. 46

Figure 6.2. Location of the gas thermocouples on the Evaporator and Post-Heater. 47

Figure 7.1. Gases' temperature results from the tests and model. 53

Figure 7.2. Water temperature results from the tests and model. 53

Figure 7.3. Power transferred in the Post-Heater for various levels of burner power. 55
Figure 7.4. Fluid temperature in the Evaporator for a burner power of 21,5 kW. 56
Figure 7.5. Fluid temperature in the Evaporator for a burner power of 16,7 kW. 57
Figure 7.6. Gas temperature for a burner power of 30,3 kW. 58

Figure B. 1. Flow-chart of the evaporator model. The iterative process controlled by the variable *variation* also applies to the one used on the post-heater model, where the control variable is named *error*. 67

Figure E. 1 Working diagram of the complete ORC prototype. 73

LIST OF TABLES

Table 5.1. Maximum fin tip and tube's exterior temperature on the Post-Heater. 33
Table 5.2. Maximum fin tip and tube's exterior temperature on the Evaporator. 33
Table 5.3. Simulation parameters for three different power levels. 34
Table 5.4. Pressure drop in the gas flow for three different power levels. 35
Table 5.5. Pressure drop in the Organic Fluid for three power levels. 36
Table 6.1. Thermocouples' characteristics. t = Measured Temperature 47
Table 6.2. Pressure sensor's characteristics. F.S = Full Scale 48
Table 6.3. Flowmeter's characteristics. 48
Table 6.4. Gas Meter's characteristics. 49
Table 6.5. Gas analyser's measurement capabilities. 49
Table 6.6. Thermometer/Hygrometer's characteristics. 49
Table 7.1. Comparison of the Power Transferred to the water for the Model and Tests. ... 52

Table A. 1. Effect of different methods for calculating gas properties on *h* (for T_film = 731 K) 66
Table A. 2 Effect of different methods for calculating gas properties on *h* (for T_film = 325 K) 66

Table C. 1. Experimental tests parameters. 69

LIST OF SYMBOLS AND ACRONYMS/ ABBREVIATIONS

List of Symbols

Variables:

C: Consumption, $m^3/300s$	$\boldsymbol{\eta}$: Efficiency
$\boldsymbol{pp}$: Partial pressure, *Pa*	$\boldsymbol{G}$: Maximum mass velocity, $kg/s.m^2$
$\boldsymbol{fma}$: Mass fraction	$\boldsymbol{cp}$: Heat capacity, *J/kg.K*
$\boldsymbol{p}$: Pressure, *Pa*	$\boldsymbol{Pr}$: Prandtl Number
$\boldsymbol{H_2O}$: Amount of Water, *mol*	$\boldsymbol{Re}$: Reynolds Number
$\mathbf{H}'$: Enthalpy, *J/mol*	$\boldsymbol{D}$: Diameter, *m*
H: Enthalpy, *J/kg*	$\boldsymbol{\mu}$: Dynamic viscosity, *Pa.s*
$\boldsymbol{\Delta h_f}$: Enthalpy of formation, *J/mol*	$\boldsymbol{A}$: Area, m^2
$\boldsymbol{Q_0}$: Energy Released in the Combustion of NG, J/mol_{NG}	$\boldsymbol{Pm}$: Perimeter, *m*
	$\boldsymbol{\sigma}$: Relation between free-flow and frontal area
P: Power, *W*	$\boldsymbol{y}$: Molar fraction
$\boldsymbol{\rho}$: Density, kg/m^3	$\boldsymbol{\varphi}$: Dimensionless quantity for properties calculations
$\boldsymbol{M}$: Molar mass, *kg/mol*	$\boldsymbol{k}$: Thermal conductivity, *W/m.K*
ṁ: Mass flow rate, *kg/s*	$\boldsymbol{Q}$: Heat transferred, *W*
$\boldsymbol{m}$: Mass, *kg*	$\boldsymbol{\varepsilon}$: Emissivity
$\boldsymbol{error}$: Difference between enthalpies (control variable), *J/*mol_{NG}	$\boldsymbol{\alpha}$: Absorptivity
	$\boldsymbol{\sigma'}$: Stefan-Boltzmann constant, W/m^2K^4
$\boldsymbol{h}$: Heat transfer coefficient, W/m^2K	$\boldsymbol{\Delta}$: Correction factor for radiation calculations
$\boldsymbol{St}$: Stanton Number	
$\boldsymbol{j_h}$: Colburn J Factor	$\boldsymbol{L_e}$: Mean beam length, *ft*
$\boldsymbol{C'}$: coefficient for absorptivity calculations	
$\boldsymbol{\eta}$: Efficiency	

$\boldsymbol{Nu}$: Nusselt Number	$\boldsymbol{X}$: Dimensionless factor for the calculation of fs
$\boldsymbol{f}$: Friction factor	$\boldsymbol{dif}$: Control variable for the evaporator model's iterative process, *J/kg*
$\boldsymbol{U}$: Overall heat transfer coefficient, W/m^2K	$\boldsymbol{\theta}$: Temperature difference between a given point on the fin and its surroundings, *K*
$\boldsymbol{Ra}$: Internal/external area ratio	$\boldsymbol{\theta_b}$: Temperature difference between the surroundings and the fin's base, *K*
$\boldsymbol{L_{CV}}$: Control volume's length, *m*	$\boldsymbol{I_0}$: Zero-order modified Bessel function of the first kind
$\boldsymbol{ARp}$: Tube wall's thermal resistance multiplied by the external area, $[m^2K/W]$	$\boldsymbol{K_0}$: Zero-order modified Bessel function of the second kind;
$\boldsymbol{R_f}$: Fouling factor, m^2K/W	$\boldsymbol{I_1}$: First order modified Bessel function of the first kind
$\boldsymbol{x}$: Vapor fraction	$\boldsymbol{K_1}$: First order modified Bessel function of the second kind
$\boldsymbol{Nc}$: Number of control volumes per tube	$\boldsymbol{r_1}$: Fin's radius at its base, *m*
$\boldsymbol{Nt}$: Number of tubes on each level	$\boldsymbol{r_2}$: Fin's radius at its tip, corrected in order to include the heat transfer in that area, *m*
$\boldsymbol{\varepsilon r}$: Relative roughness	$\boldsymbol{r}$: Fin's radius at the desired point, m
$\boldsymbol{\varepsilon a}$: Absolute roughness, *m*	$\boldsymbol{mf}$: Fin parameter, m^{-1}
$\boldsymbol{h'_{cf}}$: Forced convection coefficient, W/m^2K	**t**: Fin's thickness, *m*
$\boldsymbol{h'_{en}}$: Nucleate flow boiling coefficient, W/m^2K	$\boldsymbol{\Delta p}$: Pressure difference, *Pa*
$\boldsymbol{fc}$: Empirical parameter of *Lockhart-Martinelli*	$\boldsymbol{v}$: Specific volume, m^3/kg
$\frac{\boldsymbol{1}}{\boldsymbol{Xtt}}$: Dimensionless coefficient for the calculation of fc	$\boldsymbol{hf}$: Height of column of fluid, *m*
$\boldsymbol{h_{en}}$: Nucleate pool boiling coefficient, W/m^2K	$\boldsymbol{kp}$: Pressure loss coefficient
$\boldsymbol{fs}$: Factor which incorporates the effect of duct flow	$\boldsymbol{\Delta z}$: Height difference between two points, *m*
$\boldsymbol{h_{fg}}$: is the fluid's latent heat of vaporization, *J/kg*	$\boldsymbol{\Delta H}$: Enthalpy variation, *J/kg*
$\boldsymbol{v}$: Velocity, *m/s*	
$\boldsymbol{dp}$: Damping factor	

$\boldsymbol{F}$: Correction factor for the LMTD	$\boldsymbol{\Delta T}$: Temperature variation, *J/kg*

Subscripts:

NG: Natural Gas	$\boldsymbol{sur}$: Surface
$\boldsymbol{H_2O}$: Water	**atm**: Atmospheric
$\boldsymbol{CO_2}$: Carbon Dioxide	$\boldsymbol{fin}$: Fin/extended surface
$\boldsymbol{burner}$: NG burner	$\boldsymbol{int}$: Internal/interior
$\boldsymbol{g}$: Gas	$\boldsymbol{ext}$: External/exterior
$\boldsymbol{l}$: Liquid	$\boldsymbol{water}$: Liquid water
$\boldsymbol{sat}$: Saturation (e.g. "at Saturation pressure")	$\boldsymbol{in}$: Initial/at the entry
	$\boldsymbol{out}$: Final/at the outlet
$\boldsymbol{ref}$: Reference (e.g. "at reference temperature")	$\boldsymbol{midpoint}$: At the middle point of the Post-Heater (between the two tubes)
$\boldsymbol{R}$: Reactants	$\boldsymbol{tube}$: Heat exchanger's tubes
$\boldsymbol{P}$: Products	$\boldsymbol{level}$: Evaporator's level of tubes
T: Temperature	$\boldsymbol{new}$: Updated variable
$\boldsymbol{flame}$: Combustion flame	$\boldsymbol{O_2}$: Oxygen
$\boldsymbol{global}$: Global (includes radiation and convection)	$\boldsymbol{N_2}$: Nitrogen
	$\boldsymbol{fluid}$: Working Fluid
$\boldsymbol{rad}$: Radiative	$\boldsymbol{xf = 0}$: Saturated liquid
$\boldsymbol{conv}$: Convective	$\boldsymbol{vap}$: Vapor (saturated vapor)
$\boldsymbol{film}$: Film layer (in a flow)	$\boldsymbol{final}$: On the last CV – the evaporator's entry
$\boldsymbol{h}$: Hydraulic	$\boldsymbol{entry}$: On the real entry of the evaporator
$\boldsymbol{ff}$: Free flow	$\boldsymbol{tip}$: Tip of the fin
$\boldsymbol{mix}$: Mixture	$\boldsymbol{cond}$: Condenser
$\boldsymbol{m}$: Mean/average	

Acronyms/Abbreviations

ORC – Organic Rankine Cycle

WF – Working Fluid

CHP – Combined Heat and Power

DHW – Domestic Hot Water

NG – Natural Gas

LHV – Lower Heating Value

HHV – Higher Heating Value

CV – Control Volume

LMTD – Logarithmic Mean Temperature Difference

UC – University of Coimbra

DEM – Department of Mechanical Engineering

1. INTRODUCTION

1.1. Motivation and Objectives

It is no secret that energy is one of the main pillars that support modern civilization. It does not take much, indeed, to look around us and realise how, without the ability to transform, store and utilize energy in an effective way it would not be possible to live in the modern world as we know it. In the last few years, however, energy consumption has been growing exponentially due not only to the growth of the world's population but also to the improvement of its average quality of life. On top of this, one must notice how, as times change, what is considered "standard" and necessary for each person to lead a normal life also changes demanding an even greater energy consumption.

For these reasons, there has been an increasing level of concern about the impacts that this high energy consumption leads to. These include both environmental damage (usually in the form of greenhouse gases emissions) and the depletion of natural resources including traditional energy sources (namely fossil fuels given that their consumption occurs at a greater pace than that at which they are naturally restored). Hence the need, on top of resorting to alternative energy sources (mostly renewable ones), to make an efficient use of the ones we currently have available. It is in the latter field that we fit the concept of Cogeneration or CHP (Combined Heat and Power) and, specifically in this case, micro-CHP.

CHP or Cogeneration can be defined as the simultaneous production of thermal and electrical/mechanical energy from a single primary energy source. Generally speaking, it is similar to the production of electrical energy in a conventional way with the added benefit that the usually wasted thermal energy generated in the process will be used elsewhere (for example, in the production of domestic hot water DHW). That is when the system operates as a topping cycle. The definition provided by Decree Law no. 68-A/2015, of 30 April [1] is the following: "simultaneous production, in an integrated process, of thermal and electrical energy and, or where appropriate, mechanical". Intuitively, one can conclude that micro-CHP is nothing more than standard CHP but at a smaller scale. More

precisely, its definition (once again according to Decree Law no. 68-A/2015, of 30 April [1]) is: “small scale CHP with a power output smaller than 50 kW”. Although not specified by the Decree-Law, it is worth mentioning that these 50 kW refer to the electrical power only.

Given these definitions, it is easy to understand that these processes present a significantly higher efficiency than those traditionally used to produce electrical energy only (typically around 35% - 40%). In fact, it is possible to reach a combined total efficiency (thermal + electrical energy) of 90% or even greater which leads to large resources savings as well as lower greenhouse gases emissions. One could raise the question, however, if this this level of efficiency is sufficient given that traditional natural gas boilers may actually reach slightly higher numbers (up to approx. 95%). The answer lies in the energy quality. It is, indeed, easy to understand that the usability of thermal energy is, to say the least, very limited since it can only be used to heat a given substance/object. Electrical energy, however, has a vast field of applications (any energy requirement on a domestic level, for instance, can be satisfied with electrical power). Therefore, its quality is much higher than that of thermal energy. Additionally, partially replacing traditional power plants by these systems will avoid the complete waste of large portion of the heat generated by burning fossil fuels which is usually even larger than the amount of usable (electric) energy produced.

Due to their nature, CHP systems are usually implemented in a large scale (on and industrial level, for example) and, for this reason, are already relatively well developed and optimized for this type of purpose. Micro-CHP, on the other hand, is a relatively new concept and still lacks the high level of development and study its larger scale version has. One could be tricked into thinking that this could easily be achieved by simply reducing the size of all its components down to the desired scale. However, it is necessary to take a different approach in order to solve several challenges that this size reduction presents. Nevertheless, micro-CHP is believed to have enough potential to justify its further development and study. This potential mostly comes from the possibility of installing these systems on a domestic level for DHW/heating purposes which would result in several benefits namely a more decentralized energy production. This means greater energy supply reliability, lower losses during distribution and lower energy dependence (this is especially the case of remote areas the power network doesn’t reach). Furthermore, the residential sector has a fairly large weight on a country’s energy consumption (and, consequently, its greenhouse gases emissions) a lot of which is due to DHW. For this reason, this thesis will

have as a study object a small-scale Organic Rankine Cycle (ORC) based micro-CHP prototype whose purpose is to produce hot water for DHW and/or heating (as well as electrical energy) so that it can be applied at a residential level.

An Organic Rankine Cycle, as the name suggests, consists of a Rankine Cycle where an organic fluid is used as a WF instead of water. Generally speaking, the main difference between the two is that organic fluids tend to have a lower boiling point which justifies their use when the temperatures provided by the energy source aren't high enough to implement a traditional Rankine Cycle. For this reason, these cycles are often used to produce electricity from geothermal energy sources and also for waste heat recovery. ORCs are already fairly well developed for large and medium scale applications which means that, as previously mentioned, the main challenge will be to reduce the scale to such an extent that, ideally, the whole installation would not be much larger than a boiler or hot water cylinder typically found in a house. This would unlock the possibility of retrofitting existing dwellings with these systems. It is important to notice that a wide variety of energy sources may be used to power these cycles. These include the already mentioned waste heat and geothermal energy as well as fuels (such as biomass). In the case that will be studied here, natural gas will be the energy source since the target market (residential) is already fed (in most cases) by this type of fuel. Furthermore, in order for micro-CHP to be feasible, it is essential that the fuel used as primary energy is significantly cheaper than the electricity it will generate (at the cost of purchase) so that a potential user would benefit from a cost reduction by adopting this system.

It was previously mentioned that ORCs are commonly used when the temperatures supplied by the energy source aren't very high. However, since this system will be powered by natural gas, that will not be the case. This could also raise the question of why an organic cycle is used instead of a conventional one. It turns out working with low temperatures is not the only ORC's strength. In fact, for relatively low power installations, conventional cycles aren't able to deliver the same level of reliability and simplicity as ORCs do [2],[3], which justifies their use in cases such as this one . Nevertheless, working with a high temperature energy source will lead to one of the biggest challenges that comes from using an organic fluid: the possibility of its thermal degradation (although sources differ, it is known that at a temperature of 300°C the fluid is not subjected to any significant degradation – see [4]). Several strategies have been adopted to solve this problem, one of

which is the use of an intermediate fluid loop (with a thermal oil) in order to transfer the energy from the combustion gases to the working fluid in two steps: the gases will heat the intermediate fluid (able to withstand high temperatures) which will, in turn, transfer the thermal energy to the organic fluid at a lower temperature. This is called indirect evaporation and, even though it solves the initial problem, it is far from ideal as it leads to a worse overall efficiency (due to losses in the additional loop), a larger installation and maintenance cost (due to the added complexity and number of components) and a larger thermal inertia which could be an advantage for some cases (namely waste heat recovery) but not when the system is expected to have a short response time and highly variable working conditions. Given that DHW production is characterized by these very aspects, it is concluded that indirect evaporation is not a suitable solution for the thermal degradation problem.

The adopted solution was, therefore, the direct evaporation of the working fluid. However, instead of having the combustion gases travel directly from the burner to the evaporator, they first go through a set of finned tubes carrying water inside. This will act as a post-heater for the water coming out of the condenser which will not only lower the condenser's operating temperature (enabling the turbine to perform a more complete fluid expansion) but decrease the combustion gases' temperature as well. Therefore, it will also act as a protection for the working fluid which is expected to be enough to avoid its thermal degradation. A schematic representation of the cycle (including the evaporator and water post-heating section) is shown in Figure 1.1:

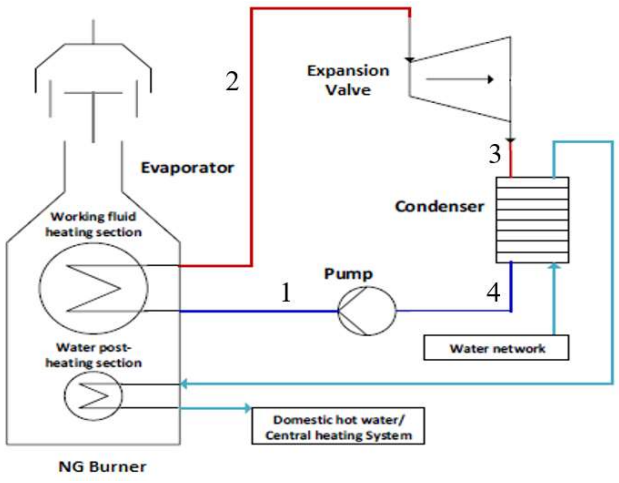

Figure 1.1. Scheme of the developed micro-CHP ORC based prototype. Adapted from [5].

Taking this into account, the main objective of this thesis is to build a mathematical model (using Matlab) which is capable of simulating the behaviour of the ORC evaporator as a whole. This will require the characterization of three separate components: the natural gas burner, the aforementioned water "post-heater" and the organic fluid evaporator itself. Needless to say, since these components are assembled in series, the outputs of the first model (the burner) will serve as inputs for the second one (the post-heater) and the same happens for the following and final model (the evaporator). In a final stage, the three models are intended to work together in order to provide useful and important dada about the behaviour of the ORC's direct evaporator, as will be specified further ahead.

1.2. State of the Art Review

Given that this is an innovative approach (the use of a direct evaporator along with a water post-heater), there hasn't been a lot of work done which can be applied in this specific case. In fact, direct vaporization has only been used for ORCs operating under lower temperatures, due to the reasons previously mentioned, while indirect evaporation has been the main choice whenever the energy sources reach high temperatures. Nevertheless, it is worth mentioning some studies conducted on ORCs which mention some of the modelling approaches that may be taken.

Liu *et al.* [6] took a theoretical look at some of the approaches for ORCs' off-design simulation, more specifically, the evaporator section. This proves to be very useful as this particular system is not intended to constantly run at optimal conditions, but instead it will respond to the highly variable hot water demands (whether it is for DHW or heating purposes). Even though the heat exchangers mentioned in this study are plate heat exchangers (typically used for indirect evaporation) it is interesting to take notice of the chosen modelling approach. In sum, the volume occupied by the working fluid is divided in three zones: liquid, two-phase and vapor. Each of which will be modelled through the use of suitable heat transfer correlations. A large amount of these correlations can be found in several tables, organized by the type of flow, fluid and heat exchanger they are adequate for.

Jiménez-Arreola *et al.* [7] published a paper where two different heat exchangers, to be used for direct evaporation in ORC waste heat recovery applications, were compared. It was mentioned that, for relatively small-scale applications where the hot fluid

is a gas, compact heat exchangers were the preferred solution with the fin-and-tube type being one of the most relevant options. It is important to notice, however, that in this particular study, a relatively high thermal inertia was desirable in order to dampen the fluctuations of the heat source (a diesel engine). Something which, as mentioned before, will not be a goal of the ORC studied in this thesis. Unlike the paper by Liu *et al.,* where the fluid contained in the evaporator was divided in three zones (depending on its phase), the method adopted here is based on a finite volume approach. This means the working fluid is discretized in a fixed number of "cells" regardless of its phase, with the calculations being performed for each individual cell. The heat transfer correlations for the fluid side are similar to those presented in the previous paper [6]. The difference lies in the ones used for the gas side as these are specific for compact heat exchangers. As of 2019, the authors have published another paper [8] where the same two direct evaporators were compared with an indirect evaporation solution, once again for waste heat recovery of a truck diesel engine and with the system's thermal inertia in main focus.

1.3. Dissertation Structure

This dissertation is organized in 8 Chapters. The 3 Chapters following the introduction consist of a description of the models elaborated for each of the three components - NG Burner, Post-Heater and Evaporator. This includes the main outputs to be provided by each one as well as the challenges faced and the strategies adopted to overcome them.

This description is followed by a parametric analysis on the results provided by these models, on Chapter 5. The behaviour of a series of important variables is presented along with an analysis and explanation of the phenomena responsible for such behaviour. In addition, this chapter includes the description of a series of small extra calculations relevant but not essential to each of the previously presented models.

Even though the constructed models and the outputs they produce already have an interest of their own, they are better supported if validated by an experimental analysis. Chapter 6 consists of a description of the test rig used to conduct these experiments as well as the procedure used to obtain the desired results.

Finally, on Chapter 7 the experimental results are compared to those produced by the model so that these can be properly validated. Beforehand, however, a quick preliminary validation is performed (on the Evaporator only) using a series of older experimental results whose process of obtention will also be briefly described.

Chapter 8 contains the conclusions of the overall performance and utility of the Models as well as recommendations for future work.

2. COMBUSTION MODEL

The first component of the ORC evaporator to be modelled is the power source which, in this case, is a pre-mixed natural gas burner. This model was developed on *MatLab* and uses *RefProp* as an auxiliary program to act as a database. Its objective is to supply values for key parameters which will be needed for the heat transfer calculations, both on the Post-Heater and the Evaporator itself. These include:

i) combustion flame temperature; ii) combustion gases' mass flow rate; iii) combustion gases' composition (namely, its components' molar fractions).

During the ORC's operation, the main input parameter (concerning the evaporator) will be the voltage supplied to the burner which controls its fan speed. For the sake of simplicity, the variable defined as main input for the model is the volumetric flow rate of natural gas which can easily be measured while performing the tests. In addition, a series of extra input variables are required to run the model, such as:

i) surrounding air temperature; ii) relative humidity; iii) natural gas' composition; iv) natural gas' supply temperature and pressure.

The level of excess of air at which the burner operates is not considered an input variable but instead a function of the NG' volumetric flow rate which, in turn, is a function of the fan's speed and input air flow rate – directly related to the burner's power output. Such dependence was determined experimentally, in previous tests. This mathematical expression was obtained using an *Excel* trend line adapted to the graph on Figure 2.1.

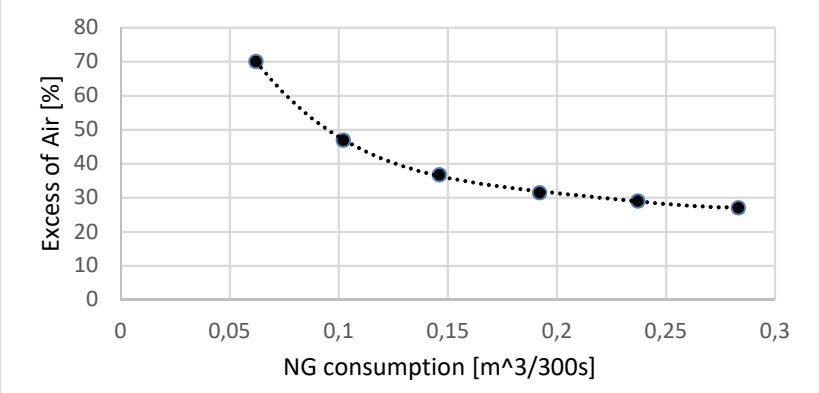

Figure 2.1. Excess of air as a function of the NG volumetric consumption.

The generated trendline is then defined by equation (2.1):

$$Excess\ of\ air = 48915{C_{NG}}^4 - 42448{C_{NG}}^3 + \\ + 13880{C_{NG}}^2 - 2091{,}7C_{NG} + 155{,}84 \quad (2.1)$$

C_{NG} being the volume of natural gas consumed over a period of 300s, value which is measured experimentally $[\mathrm{m}^3/300s]$.

In an initial step, the stoichiometric coefficients for each compound are calculated by the equation (2.2):

$$1 * (C, H, N, O) + air * (O_2 + 3{,}76N_2) = \\ = a * (CO_2) + c * (N_2) + d * (H_2O) \quad (2.2)$$

This is followed by the determination of the coefficients of the real combustion reaction which is assumed to be complete, since no CO is accounted for among the products In this step, the of excess of combustion air as well as the humidity level are considered, resulting in the equation (2.3):

$$1 * (C, H, N, O) + air' * (O_2 + 3{,}76N_2) \ + x * H_2O \ = \\ = a * (CO_2) + b * O_2 + (c * (N_2) + d * (H_2O) \quad (2.3)$$

In both this and the theoretical case, the coefficients are calculated using a simple mass balance for each of the chemical species. Once these have been determined, the mass and molar fractions of each product can be obtained as well as the partial pressures.

Since it is known that some of the water contained in the combustion gases will condense if their temperature is to drop to low values (which may occur during the ORC's regular operation), it is not wise nor is it accurate to calculate the energy released in the combustion using the LHV (lower heating value). On the other hand, it wouldn't be realistic to use the HHV (higher heating value) either since that assumes the complete condensation of all water. Therefore, the model calculates the amount of water which will condense assuming a reference temperature of 25 °C and utilizes this value to more accurately obtain the energy released in the NG's combustion.

The energy released in the combustion of natural gas - Q_0 (eq. (2.4)) is then given by the difference between the reactants and the product's enthalpy - eq. (2.5):

$$Q_0 = {H'}_{R,T} - {H'}_{P,T} \quad (2.4)$$

$${H'}_{R,T}/{H'}_{P,T} = \sum_{j=1}^{n/m} n_j \left[\Delta h_f + ({H'}_T - {H'}_{Tref})\right]_j \quad (2.5)$$

Where: $H'_{R,T}/H'_{P,T}$ [J/mol_{NG}] is the total enthalpy of the combustion reactants/products, calculated at temperature T; n/m [mol/mol_{NG}] is the number of combustion reactants/products; n_i is the amount of each compound; Δh_f [J/mol] is the enthalpy of formation of each compound; H'_T [J/mol] is the enthalpy of each compound at temperature T; H'_{Tref} [J/mol_{NG}] is the enthalpy of each compound at reference temperature; Q_0 [J/mol_{NG}] is the energy released in the combustion of 1 mol of NG.

It's in the calculation of the products' total enthalpy that the amount of condensed water will be relevant, since both liquid water and vapor are considered.

Following this step, the burner's power supply as well as the combustion gases' mass flow rate are calculated by equations (2.6) and (2.7), respectively:

$$P_{burner} = (Q_0 * C_{NG,} * \rho_{NG})/(M_{NG} * 300) \quad (2.6)$$

$$\dot{m}_{combustion\ gases} = P_{burner}/(Q_0/m_{combustion\ products,per\ kmol\ NG}) \quad (2.7)$$

P_{burner} [W] is the power delivered by the natural gas burner; ρ_{NG} [kg/m^3] is the natural gas' density at its supply temperature; M_{NG} [kg/mol]; is the natural gas' molar mass; $\dot{m}_{combustion\ gases}$ [kg/s]; is the combustion gases' mass flow rate; $m_{combustion\ products,per\ mol\ NG}$ [kg/mol_{NG}] is the total mass of the combustion products per mol of NG;

Finally, the model proceeds to calculate the combustion flame temperature. This is achieved by an iterative process where the product's enthalpy at flame temperature (initially an arbitrary value) is compared to the previously calculated reactants' enthalpy. This difference is stored in a "*error*" variable which, once below a pre-determined value, will cause the cycle to end. Equation (2.8) shows how it's obtained:

$$error = H_{R,T} - H_{P,Tflame} \quad (2.8)$$

- $H_{P,Tflame}$ [J/mol_{NG}] is the total enthalpy of the combustion reactants/products, calculated at flame temperature; $error$ [J/mol_{NG}] is the control variable of the iterative process.

While this value doesn't approach 0, it will act as a parameter used to update the flame temperature for the following iteration. The final flame temperature is determined once the products' enthalpy equals/approaches that of the reactants, causing the iterative process to end.

3. POST-HEATER MODEL

The post-heater is a heat exchanger located between the natural gas burner and the ORC evaporator which consists of a pair of finned tubes in a cross-flow configuration. These tubes will carry water which previously travelled through the condenser. The model's main objective is to accurately predict the increase in the water's temperature (and, consequently, the power transferred in the post-heater) as well as the decrease in the flue gases' temperature. Therefore, the input variables will include some of the Combustion Model's outputs such as:

i) combustion flame temperature; ii) combustion gases' mass flow rate; iii) combustion gases' composition.

Additionally, it is necessary to know some information concerning the water which enters the post-heater, namely:

i) water temperature; ii) water mass flow rate; iii) water pressure.

Since it is known that not only will the water inside the tubes remain in the liquid state but also its temperature will not rise drastically, the system was simply divided in two control volumes (CV) – one for each tube, as shown in Figure 3.1. Only one CV is considered on the gas side as, due to a series of phenomena (convection in the gas flow, turbulence, etc.), its temperature distribution is considered even in a horizontal direction.

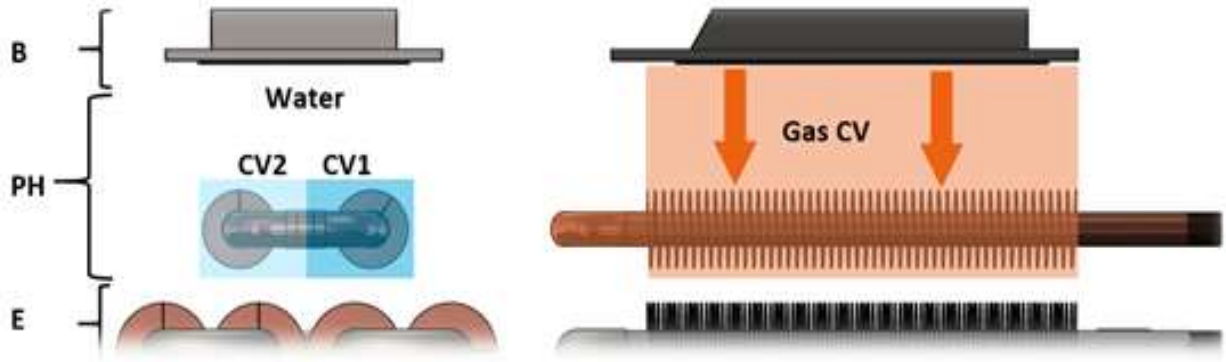

Figure 3.1. 2D view of the burner (B), post-heater (PH) and evaporator (E) assembly with the control volumes defined for both the water and gas flow.

In order to determine the overall heat transfer coefficient *U*, it is first necessary to obtain the heat transfer coefficient (h) for both the water and gas' side (internal and external, respectively).

The external heat transfer coefficient is separated in two components: the convective heat transfer coefficient - $h_{conv,g}$ and the radiative heat transfer coefficient - $h_{rad,g}$. Since the heat exchanger's walls are assumed to be at the same temperature as the flue gases (which results from considering them adiabatic), these two can simply be added [9], resulting in the "global" heat transfer coefficient $h_{global,g}$, given by the equation (3.1):

$$h_{global,g} = h_{rad,g} + h_{conv,g} \qquad [W/m^2K] \tag{3.1}$$

h_{conv} is obtained according to the method presented by *Incropera et al.* [10] on the "*Compact heat exchangers*" section. Here, the heat transfer coefficient is correlated in terms of the *Stanton number St* (3.2) and the *Colburn J factor* j_h (3.3).

$$St = h_{conv,g}/G.cp_{film,g} \tag{3.2}$$

$$j_h = St * {Pr_g}^{2/3} \tag{3.3}$$

$h_{conv,g}$ $[W/m^2K]$ is the gas' convective heat transfer coefficient; G $[kg/s.m^2]$ is the gas' maximum mass velocity; $cp_{film,g}$ [J/kg.K] is the gas's cp, evaluated at film temperature; Pr_g is the gas' Prandtl number.

The *Colburn J factor* may be obtained from a graph (see reference [10]) as a function of the Reynolds number (Re) with:

$$Re = G * D_h/\mu_g \tag{3.4}$$

$$D_h = 4A_{fr}/Pm \tag{3.5}$$

$$G = \dot{m}_g/(\sigma A_{ff}) \tag{3.6}$$

Here: D_h [m] is the hydraulic diameter of the flow zone; μ_g [Pa.s] is the gas' dynamic viscosity; A_{ff} $[m^2]$ is the free-flow area of the post-heater, that is to say, the available cross-section area the gases have to travel through; *Pm* [m]is the perimeter of that same area; $\dot{m}_g$ [kg/s] is the gas' mass flow rate; σ is the relation between the free-flow area and the total frontal area of the exchanger.

This graph (as well as all other graphs needed to obtain certain coefficients) was inserted in the model with the help of an *Excel* trendline. All the combustion gases' properties are evaluated at average film temperature (the average between the actual gases' temperature and that of the tubes' external surface).

Since the combustion gases consist of a mixture of several substances, it is necessary to calculate the properties of the whole mix (once the properties for each individual component have been obtained). While the density and c_p values may be calculated by simple molar and mass weighted averages (respectively), the same cannot be done for the thermal conductivity and dynamic viscosity due to the fact that the way the properties of different gases influence each other is more complex. These calculations can be found in Annex A.

The final step in the calculation of the convective heat transfer coefficient is the introduction of a correction factor. According to the "*Flow Across Banks of Tubes*" section (*Incropera et at*., [10]), in a gas flow across a bank of tubes (either aligned or staggered) the first rows/levels act as a turbulence generator which will increase heat transfer in the following levels. According to the authors, this effect stabilizes after four or five levels, meaning that no correction factor is necessary if this number is relatively large. Even though the post-heater only has one level of tubes, it is located directly above the evaporator which has four, leading to a five level staggered tubes configuration. Therefore, each value of $h_{conv,g}$ (one for the post-heater and four for the evaporator) is multiplied by the adequate correction factor which becomes larger as the gas moves through each level.

Once the convective heat transfer coefficient has been determined, the model proceeds to calculate the radiative heat transfer coefficient $h_{rad,g}$. This value is obtained by setting two equations of heat transfer by radiation between a gas and a surface equal to each other.

$$Q_{rad} = A * h_{rad} * (T_{m,g} - T_{sur}) \tag{3.7}$$

$$Q_{rad} = A * \sigma' * (\varepsilon_g * {T_{m,g}}^4 - \alpha_g * {T_{sur}}^4) \tag{3.8}$$

Where: Q_{rad} [W] is the power transferred by radiation; A [m^2] is the total heat transfer area; $T_{m,g}\,[K]$ is the mean gas temperature [K]; T_{sur} [K] is the surface's mean

temperature; σ' $[W/m^2K^4]$ is the *Stefan-Boltzmann* constant; ε_g is the gases' emissivity; α_g is the gases' absorptivity.

In order to obtain these parameters, the method proposed by *Incropera et al.* [10] on the "*Gaseous Emission and Absorption section*", was followed. Here, equation (3.9) is used to calculate the emissivity of a gas mixture containing water and carbon dioxide (as well as nonradiating species such as oxygen and nitrogen):

$$\varepsilon_g = \varepsilon_w + \varepsilon_c - \Delta_\varepsilon \tag{3.9}$$

ε_g is the gas mixture emissivity; ε_w is the emissivity of water vapor; ε_c is the emissivity of carbon dioxide; Δ_ε is a correction factor which accounts for the interaction between the two radiating species present.

Beforehand, however, it is necessary to determine the so-called Mean Beam Length L_e which is a characteristic of the space the gas occupies' geometry. It is defined, in this case (arbitrary shape of volume V radiating to surface of area A) by the equation (3.10):

$$L_e = \frac{3.6V}{A} * 3{,}28084 \qquad [ft] \tag{3.10}$$

Once this value has been obtained, the following sequence of steps is used to calculate the gas mixture's emissivity:

i) evaluation of ε_w through the graph in Figure 13.15 [10] using $pp_{H_2O} * L_e$ and $T_{m,g}$ as entry parameters (pp_{H_2O} in *atm*, L_e in *feet* and $T_{m,g}$ in K); ii) evaluation of ε_c through the graph in Figure 13.17 [10] using $pp_{CO_2} * L_e$ and $T_{m,g}$ as entry parameters (pp_{H_2O} in *atm*, L_e in *feet* and $T_{m,g}$ in K); iii) evaluation of Δ_ε through the graph in Figure 13.19 [10] using $(pp_{H_2O} + pp_{CO_2}) * L_e$ and $\frac{pp_{H_2O}}{pp_{Co2} + pp_{H_2O}}$ as entry parameters; iv) finally, the gas mixture's emissivity is given by the equation (3.9).

Similarly, the gases' absorptivity α_g is determined by the equation (3.11):

$$\alpha_g = \alpha_w + \alpha_c - \Delta_\alpha \tag{3.11}$$

Where $\Delta_\alpha = \Delta_\varepsilon$ and

$$\alpha_w = C'_w * \left(\frac{T_{m,g}}{T_{sur}}\right)^{0.45} * \varepsilon_w' \tag{3.12}$$

$$\alpha_c = C'_c * \left(\frac{T_{m,g}}{T_{sur}}\right)^{0.65} * \varepsilon_c' \quad (3.13)$$

α_w is the absorptivity of water vapor; α_c is the absorptivity of carbon dioxide; Δ_α is a correction factor which accounts for the interaction between the two radiating species present; ε_w' and ε_c' are obtained similarly to ε_w and ε_c with the difference that, while consulting the respective graphs, the entry parameters are altered. $T_{m,g}$ is replaced by T_{sur} (the tube's external temperature was used) and $pp_{H_2O} * L_e$ and $pp_{CO_2} * L_e$ are replaced, respectively, by $pp_{H_2O} * L_e * \frac{T_{sur}}{T_{m,g}}$ and $pp_{CO_2} * L_e * \frac{T_{sur}}{T_{m,g}}$.

The coefficients C'_w and C'_c are evaluated from the graphs on figures 13.16 and 13.18 from [10], respectively.

The last step necessary to determine the overall heat transfer coefficient, which concerns the gas' side, is the fin's efficiency. The overall surface efficiency η_{sur} which characterizes the behaviour of an array of fins attached to a base surface is calculated using equation (3.14):

$$\eta_{sur} = 1 - \frac{A_{fin}}{\mathrm{A}}\left(1 - \eta_{fin}\right) \quad (3.14)$$

Where: A_{fin} $[m^2]$ is the total fin area; A $[m^2]$ is the total heat transfer area; η_{fin} is the efficiency of each individual fin which can be obtained using the graph from Figure 3.20 of reference [10] (approximated with an Excel trendline).

Once the calculations concerning the gas side have been completed, the next step will be the determination of the internal heat transfer coefficient h_{water} - equation (3.15):

$$h_{water} = Nu_D * k_{water}/D_{int} \quad (3.15)$$

As seen in the equation, this coefficient is a function of: the tube's internal diameter D_{int} [m]; water's thermal conductivity K_{water} [W/m.K]; the Nusselt number Nu_D. The latter is calculated using the *Gnielinski* correlation (see [10]), given by equation (3.16):

$$Nu_D = \frac{\left(\frac{f}{8}\right)(Re_D - 1000)Pr}{1 + 12.7\left(\frac{f}{8}\right)^{\frac{1}{2}}(Pr^{\frac{2}{3}} - 1)} \quad (3.16)$$

where: Re_D is the Reynolds number of the water flow inside the tubes; Pr is the Prandtl number of water; f is a friction factor which, for smooth tubes, is given by eq. (3.17):

$$f = (0{,}79\ln(Re_D) - 1{,}64)^{-2} \tag{3.17}$$

All the aforementioned water properties are evaluated the fluid's mean (not film) temperature. This is probably due to the fact that the *Gnielinski* correlation is adequate for turbulent flow (which will, indeed, occur in the Post-Heater). On this type of flow, due to its nature, the radial temperature distribution will be more even than on laminar flow which explains the lack of need to use the film temperature to evaluate these properties.

Additionally, as previously mentioned, the system was divided in two control volumes which means that these calculations will be done separately for each CV. Consequently, there will also be two different values for the overall heat transfer coefficient *U* whose calculation will now be explained.

It was decided that *U* would be calculated relatively to the gas' side in order to facilitate the incorporation of the fins' effect (found on the tubes' outer surface). Therefore, it will be represented by U_g. The steps used to reach this result are the following:

Firstly, the ratio between the internal and external heat transfer area (Ra) is determined (equation (3.18)) followed by the thermal resistance of the tube's wall multiplied by the external area (ARp_i) – eq. (3.19).

$$Ra = \pi * D_{int} * L_{CV}/A \tag{3.18}$$

$$ARp_i = \frac{D_{int} * ln(D_{ext}/D_{int})}{2 * k_i * \mathrm{Ra}} \tag{3.19}$$

Where: Ra is the internal/external area ratio; L_{CV} [m] is the length of each control volume; ARp_i $[m^2K/W]$ is the wall's thermal resistance multiplied by the external area (for each control volume); D_{ext} [m] is the tube's external diameter; k_i [W/m.K] is the thermal conductivity of the tube for each control volume; i is an index for each CV (1,2).

Now, the value of $U_{g,i}$ for each control volume can be obtained (in W/m^2K) using the equation (3.20):

$$U_{g,i} = \frac{1}{\frac{1}{h_{water\ i} * \mathrm{Ra}} + \frac{R_{f\ int}}{\mathrm{Ra}} + ARp_i + R_{f\ ext} + \frac{1}{h_{global,g} * \eta_{sur}}} \tag{3.20}$$

With $R_{f\ int}$ and $R_{f\ ext}$ $[m^2K/W]$ representing, respectively, the internal and external fouling factors.

Having determined these two values, it is possible to calculate the power transferred from the combustion gases to the water using equation (3.21):

$$Q_i = U_{g,i} * A * (T_{m,g} - T_{m\,water,i}) \tag{3.21}$$

Where: Q_i [W] is the power transferred in the VC i ; $T_{m\,water,i}$ [K] is the mean water temperature inside each CV.

Finally, the initially arbitrary values for both the gases' and the water's temperature at the Post-Heater's exit may be recalculated (equations (3.24) and (3.23), respectively). These will be of extreme importance for the convergence of the iterative process used, which will be explained further ahead.

$$T_{midpoint,water} = \frac{Q_1}{\dot{m}_{water} * cp_{water,1}} + T_{in,water} \tag{3.22}$$

$$T_{out,water} = \frac{Q_2}{\dot{m}_{water} * cp_{water,2}} + T_{midpoint,water} \tag{3.23}$$

$$T_{out\,g,i} = T_{flame} - \frac{Q_i}{\dot{m}_g * cp_{m,g}/2} \tag{3.24}$$

Where: $T_{midpoint,water}$ [K] (3.22) is the water temperature between the two tubes of the Post-Heater – the middle point in the water's path; $\dot{m}_{water}$ [kg/s] is the mass flow rate of water; $cp_{water,i}$ [J/kg.K] is the cp of water on CV *I*; $T_{in,water}$[K] is the water temperature at the inlet; $T_{out,water}$ [K] is the water temperature at the outlet; $T_{out\,g,i}$ [K] is the gas' temperature after going through CV i; T_{flame} [K] is the combustion flame temperature; $cp_{m,g}$ [J/kg.K] is the gas' cp evaluated at mean temperature.

Since the gases' outlet temperature is assumed to be uniform, an arithmetic mean is calculated on the two values of $T_{out\,g,i}$, resulting in a single outlet temperature.

Another value which is required to properly run the following iteration is the tubes' exterior temperature (eq. (3.25) as it is used to calculate the gas' film temperature). Additionally, the interior temperature is also calculated (eq. (3.26)) as it may be used as reference for the maximum fluid temperature (on its boundary layer).

$$T_{tube\,ext,i} = Q_i * (\frac{1}{h_{water\,i} * A_{int}} + \frac{R_{f\,int}}{A_{int}} + Rp_i) + T_{m\,water,i} \tag{3.25}$$

$$T_{tube\,int,i} = Q_i * \frac{1}{h_{water\,i} * A_{int}} + T_{m\,water,i} \tag{3.26}$$

Where: $T_{tube\ ext,i}$ [K] is the tube's mean exterior temperature; A_{int} $[m^2]$ is the interior area of the tube; Rp_i [K/W] is the wall's thermal resistance and $T_{tube\ int,i}$ is the tube's mean interior temperature on CV *i* [K].

After this step, the value for the copper's thermal conductivity is updated using the calculated tubes' external temperatures along with a second order polynomial function (constructed using *Excel*).

As previously mentioned, this mathematical model is based on an iterative process. The need to do so arises from the fact that there are some initially unknown parameter values (such as the gas and water outlet temperatures, tubes' exterior temperatures, material's conductivity, etc.) which are needed for the calculations performed. Once an iteration has been completed, these unknown values will have been updated based on the results obtained. A new iteration is performed where these will be used to obtain new results and this cycle will go on until they stabilize between iterations.

This is performed with the use of a *while* cycle and a control variable named *error*. This variable will measure the difference (in K) between the two values obtained in two consecutive iterations for the water's outlet temperature. The cycle ends once this variable reaches below a pre-established value (which may be changed according to the desired accuracy). When describing the evaporator model on the next chapter, a flowchart will be presented in order to demonstrate the working principles behind the model. A similar iterative process to the one just described will be included on this chart as the evaporator model requires the use of such cycle (as well as others) in order to complete a simulation. The only difference being that the variable named *error* (on the post-heater's model) will be called *variation* on the evaporator's.

Once this iterative process has been completed, the total power transferred is calculated by simply adding that of each CV, being this the final step of the Post-Heater model.

4. EVAPORATOR MODEL

4.1. Overview and Heat Transfer Calculations

The main objective of this thesis work is to simulate the behaviour of the ORC's evaporator. This essentially consists of a compact heat exchanger of a mixed configuration. That is to say, the two fluids do not run in a counter-flow path nor do they run in a purely crossflow configuration. This can be demonstrated by Figure 4.1.

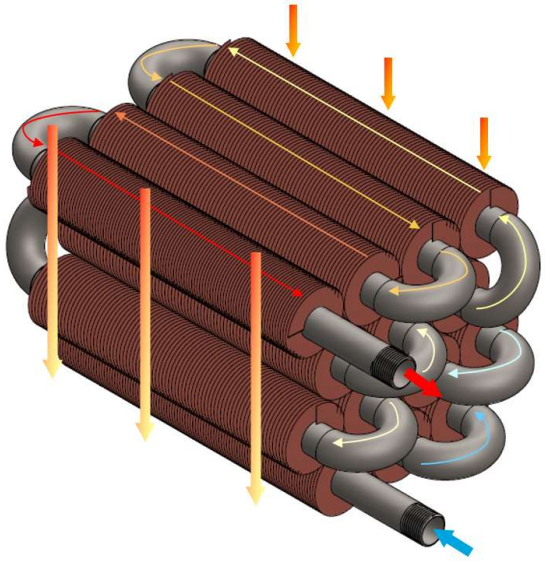

Figure 4.1. Isometric view of the evaporator section. The working fluid runs inside the tubes, in the direction of the arrows, while the gas flows on their exterior.

As demonstrated, the evaporator contains 4 "levels" of stainless-steel tubes with copper fins. Each level contains a different number of tubes, as shown by Figure 4.2.

In a similar fashion to the Post-Heater model, this one will require a series of input variables in order to run a simulation, some of which will result from the two previous models, namely:

i) flue gases' temperature (from the Post-Heater model); ii) flue gases' mass flow rate (from the Combustion model); iii) flue gases' composition (from the Combustion model).

While others will concern the organic fluid's entry conditions:

i) fluid temperature; ii) fluid mass flow rate; iii) fluid pressure.

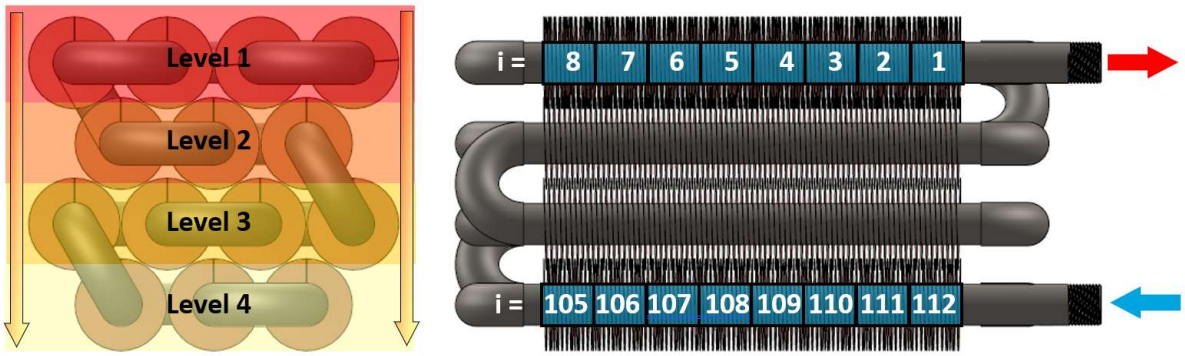

Figure 4.2. 2D view of the evaporator section with the discretization of the gas and fluid flow per control volumes. For this scheme, it was considered *Nc* =8 and only the first and last tubes' CVs are shown.

The organic fluid to be used in this system is *Pentafluoropropane*, also known as *R-245fa*. In spite of this, the model is intended to accurately simulate the behaviour of this heat exchanger regardless of the exact fluid chosen. Therefore, one of the input variables will be the type of fluid used.

This model is expected to provide a series of important outputs, such as:

- Fluid's final temperature (as well as its evolution as it travels through the exchanger);
- Gases' temperatures after each of the four levels;
- Power transferred in each level;
- Tube's internal temperature (which will serve as reference for the maximum fluid temperature, on its boundary layer).

The approach required to construct this model is, in part, different than the one used for the Post-Heater. This is due to the fact that the organic fluid will enter the evaporator as a liquid and, naturally, change phase and leave as vapor. Furthermore, the heat exchanger doesn't have a simple crossflow configuration, as previously shown. In order to tackle these problems, the total volume of organic fluid inside the evaporator was split in a large number of CVs. The input variable *Nc* controls the number of CVs per tube (for a total of 14 tubes). This number can be adjusted according to the desired accuracy of each simulation. The volume occupied by the gases was split in four – one per level. Additionally, since the path

the fluid and the gases travel through is somewhat in opposite directions, the organic fluid's final temperature (and not initial) was considered, in a first stage, an input variable in order to facilitate the construction of the model. This means that the fluid's control volumes are run in the opposite direction of the real flow, as Figure 4.2 clearly demonstrates.

The calculations concerning the gas side were performed almost exactly like on the Post-Heater model with a few exceptions. Therefore, the determination of the gas' properties, $h_{rad,g}$, $h_{conv,g}$, $h_{global,g}$ and the fins' efficiency will not be explained in this chapter. The difference here lies in the fact that these calculations will be performed four times – once per level. The exit temperature from one level will serve as the entry temperature for the following.

Once again, there are some unknown variables (such as the gases' temperature at the exit of each level, the tubes' temperatures and the copper and stainless steel's conductivity) which will have to be arbitered for the first iteration and later replaced by the real values.

The main difference in the calculations concerning the gas side is the way the film temperature is obtained. Instead of calculating an average between the gases' and the tubes' mean temperatures, a logarithmic mean temperature difference (LMTD) is used. This change arises from the fact that there will be a significant variation in the gases' temperature. On top of this, and unlike with the Post-Heater, there are levels where the lowest temperatures reached by the gases will come close to that of the fluid's (and, therefore, the tubes'). In these cases, using a simple average won't produce accurate results as it oversimplifies the evolution of the gas' temperature. The exact way this calculation is performed can be seen in equation (4.1):

$$T_{film\ g,level} = T_{tube\ ext,level} + \frac{(T_{g\ in,level} - T_{tube\ ext,level}) - (T_{g\ out,level} - T_{tube\ ext,level})}{\ln\left(\frac{T_{g\ in,level} - T_{tube\ ext,level}}{T_{g\ out,level} - T_{tube\ ext,level}}\right)} \quad (4.1)$$

Where: $T_{film\ g,level}$ [K] is the film temperature of the gases on each level; $T_{tube\ ext,level}$ [K] is the tubes' mean exterior temperature on each level; $T_{g\ in,level}$ [K] is the gases' entry temperature on each level; $T_{g\ out,level}$ [K] is the gases' exit temperature on each level.

As previously mentioned, the fluid's side is divided in *Nc* control volumes per tube, meaning that each level will have *Nc*Nt* CVs (*Nt* being the number of tubes per level, which as specified above). A cycle was created in order to run through all CVs with the index *i* [1 : *Nc**14] indicating the number of each control volume. The level number is indicated by the index variable *level* [1 : 4]. Through the use of *if* conditions together with *while* cycles, the model will switch levels after the last CV of each level has been reached.

In sum, the sequence of steps for each individual CV's calculations is the following:

- Evaluate the phase the fluid finds itself in (liquid, two-phase, vapor) - xf through the use of the *RefProp* program (fluid pressure p_{fluid} and enthalpy $H_{fluid\ in,i}$ as entry parameters):
- Utilize the adequate correlations, according to the fluid's phase, in order to obtain the internal convection coefficient (this step will be explained in greater detail further ahead);
- Calculate the overall heat transfer coefficient, relatively to the gas' side, for that specific CV – equation (4.2):

$$U_{g\,i} = \frac{1}{\frac{1}{h_{fluid\,i} * \mathrm{Ra}} + \frac{R_{f\,int}}{\mathrm{Ra}} + ARp_i + R_{f\,ext} + \frac{1}{h_{global\,g,level} * \eta_{sur,level}}} \tag{4.2}$$

- All parameters have the same meaning as in the Post-Heater model with $h_{fluid\,i}$ $[W/m^2K]$ representing the internal heat transfer coefficient.

- Calculate the power transferred in that CV using, once again, the logarithmic mean temperature difference – equation (4.3).

$$Q_i = U_{g\,i} * A * F * \frac{\left(T_{g\,in,level} - T_{fluid\,in,i}\right) - \left(T_{g\,out,level} - T_{fluid\,in,i}\right)}{\ln\left(\frac{T_{g\,in,level} - T_{fluid\,in,i}}{T_{g\,out,level} - T_{fluid\,in,i}}\right)} \tag{4.3}$$

$T_{fluid\,in,i}$ [K] is the fluid's entry temperature on each CV; *F* is the correction typically factor used with the LMTD which, in this case, is equal to 1.

- Calculate the fluid's (4.4) and gases' (4.5) enthalpy at the exit of the CV:

$$H_{fluid\,out,i} = H_{fluid\,in,i} - Q_i/\dot{m}_{fluid} \tag{4.4}$$

$$H_{g\ out\ i} = \frac{H_{g\ in,level} * \dot{m}_{g\ in,level} - Q_i * (Nc * Nt)}{\dot{m}_{g\ out,level}} \quad (4.5)$$

Where: $H_{fluid\ out,i}$ [J/kg] is the fluid's enthalpy at the exit of each CV; $H_{fluid\ in,i}$ [J/kg] is the fluid's enthalpy at the entry of each CV; $\dot{m}_{fluid}$ [kg/s] is the fluid's mass flow rate; $H_{g\ out\ i}$ [J/kg] is the gas' enthalpy at the exit of each CV; $H_{g\ in,level}$ [J/kg] is the gas' enthalpy at the entry of each level; $\dot{m}_{g\ in,level}$ [kg/s] is the gas' mass flow rate at the entry of each level; $\dot{m}_{g\ out,level}$ [kg/s] is the gas' mass flow rate at the exit of each level.

- Calculate the internal ($T_{tube\ int,i}$) and external ($T_{tube\ ext,i}$) tube temperature for that CV – equations (4.6) and (4.7), respectively:

$$T_{tube\ int,i} = Q_i \left(\frac{1}{h_{fluid\ i} * A_{int}} \right) + T_{fluid\ in,i} \quad (4.6)$$

$$T_{tube\ ext,i} = Q_i \left(\frac{1}{h_{fluid\ i} * A_{int}} + \frac{R_{f\ int}}{A_{int}} + Rp_i \right) + T_{fluid\ in,i} \quad (4.7)$$

- Determine the fluid's temperature at the exit of the CV, using its enthalpy and the *RefProp* program.
- Update the stainless steel's thermal conductivity using the previously determined value along with a second order polynomial function.

At the end of each CV, parameters like the fluid's exit temperature and enthalpy are transformed into the entry parameters for the following CV and so on.

Once all of the control volumes in one level have been run through, an arithmetic average is calculated out of all of the tubes' exterior temperatures as well as the gases' enthalpy (since these values have to be uniform for each level in order to calculate the gas' properties). The latter is used to calculate, by an iterative process, the gases' temperature which, on top of being the initial temperature for the next level, will be stored for the next iteration (since the values initially used were arbitrary). Additionally, the total power transferred in that level is calculated. This is performed for both the gases (4.9) and the fluid (4.10). Assuming no thermal losses are considered, these results should be the same.

$$Q_{fluid,level} = (H_{fluid\ in,level} - H_{fluid\ out,level}) * \dot{m}_{fluid} \quad (4.8)$$

$Q_{fluid,level}$ [W] is the total power received by the fluid in one level; $H_{fluid\ in,level}$ [J/kg] is the initial fluid enthalpy of the first CV on that level; $H_{fluid\ out,level}$ [J/kg] is the final fluid enthalpy of the last CV on that level.

It is important to take notice that the words "in" and "out", when referring to the fluid, are according to the direction the CVs are run through which is opposite to the direction the fluid actually flows through (Figure 4.2). This means that both the fluid's and the gases' enthalpy will decrease from one CV/level to the other.

The power transferred from the gases is:

$$Q_{g,level} = H_{g\ in,level} * \dot{m}_{g\ in,level} - H_{g\ out,level} * \dot{m}_{g\ out,level} \quad (4.9)$$

$Q_{g,level}$ [W] is the power lost by the gases in one level; $H_{g\ out,level}$ [J/kg] is the gases' enthalpy at the exit of each level, calculated by averaging $H_{g\ out,i}$; $\dot{m}_{g\ out,level}$ [kg/s] is the gases' mass flow rate at the end of each level.

As it may be observed, two different values of the gases' mass flow rate are used (one for the level's entry and another for its exit). This is due to the fact that, in some cases, the temperatures reached by the gases may be so low that condensation may occur. In those cases, it is considered that as part of the water condenses, it is removed from the mixture, reducing its mass flow rate. Nonetheless, this consideration implies an approximation as the condensed water still has some energy (even if very little compared to vapor).

Additionally, the reduction in the amount of water vapor contained in the gases will lead to a change in all the components' partial pressures, mass and molar fractions. All of which have to be re-calculated.

$$y_{water,g} = \frac{p_{sat\ water}}{pp_{\ water}} * y_{water} \quad (4.10)$$

$$y_{water,l} = y_{water} - y_{water,g} \quad (4.11)$$

Where: $y_{water,g}$ is the molar fraction of water which remains in a gaseous state; $p_{sat\ water}$ [Pa] is the saturation pressure of water at the gases exit temperature; $pp_{\ water}$ [Pa] is the initial partial pressure of water; y_{water} is the initial molar fraction of water; $y_{water,l}$ is the molar fraction of water which will condense.

$$m_{g\ out,level} = m_{g\ in,level} - m_{g\ in,level} * fma_{\ water} * \left(1 - \frac{p_{sat\ water}}{pp_{water}}\right) \quad (4.12)$$

With $fma_{\ water}$ representing the mass fraction of water.

Now, the new molar fraction of water ($y_{water,new}$) can be calculated – eq. (4.13):

$$y_{water,new} = \frac{y_{water,g}}{y_{CO_2} + y_{O_2} + y_{N_2} + y_{water,g}} \quad (4.13)$$

The molar fractions of the remaining components as well as the new mass fractions may be calculated in a similar way. These will serve as the initial value for the following level, if there is one.

At the end of each level, the copper's thermal conductivity will also be updated as it is necessary for the fin's efficiency.

Another important remark is that a simplification was made while calculating the power transferred. Instead of using the initial and final fluid temperature in each CV (to obtain its properties and calculate the heat transfer), only the initial temperature is considered. This eliminates the need to arbitrate an extremely high amount of values (the fluid's temperature at the exit of each CV) as it could cause instability problems. Furthermore, no correction factor *F* (4.3) will have to be used when calculating the LMTD since, by assuming a constant fluid temperature, the heat exchanger's configuration becomes irrelevant (just like an evaporator or condenser). This simplification is considered acceptable due to the large number of control volumes which makes their individual length very small and, therefore, the variation in the fluid's temperature small as well.

4.2. Internal Heat Transfer Coefficient

Now moving to a more detailed description of the internal convection coefficients calculations, two distinct cases can be found:

- The organic fluid is in a single-phase flow (whether it's liquid or vapor). In this case, the *Gnielinski* correlation is used once again – equation (3.16), now adapted to the fluid with f being given by equation (4.14) since the tubes are no longer considered smooth.

$$f = \frac{1}{(1{,}8 \log\left(\frac{6{,}9}{Re_D}\right) + \left(\frac{\varepsilon r}{3{,}7}\right)^{1{,}11})^2} \quad (4.14)$$

With the relative roughness εr defined by equation (4.15):

$$\varepsilon r = \varepsilon a / D_{int} \quad (4.15)$$

εa [m] being the tube's absolute roughness.

- The organic fluid is in a two-phase flow:

This case will require a different approach, with the method used by *André et al.* [11] being adopted. Now, the internal convection coefficient (h_{fluid}) is given by the sum of the forced convection coefficient (h'_{cf}) with the nucleate flow boiling coefficient (h'_{en}) – eq. (4.16):

$$h_{fluid} = h'_{en} + h'_{cf} \qquad [W/m^2K] \tag{4.16}$$

With h'_{cf} given by equation (4.17):

$$h'_{cf} = h_{int,x=0} * fc \qquad [W/m^2K] \tag{4.17}$$

Where: $h_{int,\ x=0}\,[W/m^2K]$ is the internal convection coefficient considering saturated liquid ($x = 0$); fc is the empirical parameter of *Lockhart-Martinelli* for a turbulent two-phase flow, defined by equation (4.18):

$$fc = 10^{0,08021*log^2\left(\frac{1}{X_{tt}}\right)+0,54727*\log\left(\frac{1}{X_{tt}}\right)+0,45327} \tag{4.18}$$

Which is valid if $0,1 \leq \frac{1}{Xtt} \leq 100$, with $\frac{1}{Xtt}$ given by equation (4.19):

$$\frac{1}{Xtt} = \left(\frac{x}{1-x}\right)^{0,9} * \left(\frac{\rho_{f\ liq}}{\rho_{f\ vap}}\right)^{0,5} * \left(\frac{\mu_{f\ vap}}{\mu_{f\ liq}}\right)^{0,1} \tag{4.19}$$

Where: x is the vapor fraction; $\rho_{fluid\ liq}\,[kg/m^3]$ is the fluid's density, considering saturated liquid; $\rho_{fluid\ vap}\ [kg/m^3]$ is the fluid density, considering saturated vapor; $\mu_{fluid\ liq}$ [Pa.s] is the fluid's dynamic viscosity, considering saturated liquid; $\mu_{fluid\ vap}$ [Pa.s] is the fluid's dynamic viscosity, considering saturated vapor;

While running the simulations, it was verified that the parameter $\frac{1}{Xtt}$ may go beyond the aforementioned interval in the first one or two CVs with two-phase flow (where x is high, since the CVs are run in an opposite direction to the fluid's flow). However, since during the fluid's evaporation the thermal resistance on the gas' side (even with the fins) is much larger than on the fluid's side, it is the value of $h_{global,g}$ which will control U_g the most. This means that potentially having one or two values of h_{fluid} higher than in reality will not have a significant impact on the heat transfer (especially given the small CV's size).

The nucleate flow boiling coefficient (h'_{en} – equation (4.20)) is obtained by multiplying the nucleate pool boiling coefficient (h_{en}) by a factor (fs) which incorporates the effect of duct flow.

$$h'_{en} = h_{en} * fs \qquad [W/m^2K] \tag{4.20}$$

h_{en} may be calculated using the *Forster and Zuber* correlation – eq. (4.21):

$$h_{en} = 0{,}00122 \frac{{k_{fluid\ liq}}^{0,79} * {cp_{fluid\ liq}}^{0,45} * {\rho_{fluid\ liq}}^{0,49}}{{\sigma_f}^{0,5} * {\mu_{fluid\ liq}}^{0,24} * {h_{fg}}^{0,24} * {\rho_{fluid\ vap}}^{0,24}} * \\ * \left(T_{tube\ int} - T_{fluid\ sat}\right)^{0,24} * \left(p_{fluid\ sat\ @}\,(T_{tube\ int}) - p_f\right)^{0,75} \tag{4.21}$$

Where: $k_{fluid\ liq}$ [W/m. K] is the fluid's thermal conductivity considering a liquid state; $cp_{fluid\ liq}$ $[J/kg.K]$is the fluid's *cp* considering a liquid state; σ_{fluid} [N/m] is the fluid's surface tension; h_{fg} [J/kg] is the fluid's latent heat of vaporization; $T_{fluid\ sat}$ [K] is the fluid's saturation temperature; $p_{fluid\ sat\ @}\,(T_{tube\ int})$ is the fluid's saturation pressure at the tube's interior temperature [kPa]; p_{fluid} is the fluid's pressure [kPa].

The fs factor is given by equation (4.22):

$$fs = 0{,}14625 * log^3(X) - 2{,}0917 * log^2(X) + 9{,}3687 * \log(X) - 12{,}459 \tag{4.22}$$

With

$$X = Re_l * fc^{1,25} \tag{4.23}$$

and

$$Re_l = \frac{(1-x) * \rho_f * v_{fluid} * D_{int}}{\mu_{f\,l}} \tag{4.24}$$

- ρ_f $[kg/m^3]$ is the fluid's density;
- v_{fluid} [m/s] is the fluid's velocity;

4.3. Final Considerations

A full iteration is considered completed once all CVs and levels have been run through. The main outputs of this iteration will be the gasses' exhaust temperature, the total power transferred (calculated exactly like it is done for each level) and the fluid's temperature at the entry of the evaporator (since the CVs have been run through in the

opposite direction the fluid travels in). At this point a new iteration is initiated where all the values that had been arbitered for the first one will be replaced by the actual results of the completed iteration. This is performed using a *while* cycle and a control variable named *variation*. This variable evaluates (after each iteration) the difference between the total power calculated in that iteration itself and that of the previous one. In a similar way to what was done in the Post-Heater model, the cycle ends once this variable reaches below a pre-determined value, meaning that the results have stabilized from one iteration to the other.

Since a logarithmic mean temperature difference, which is used to calculate the power transfer, has an asymptotic behaviour it is worth noticing that some numerical instability may occur. In order to avoid this issue and help with the iterative process' convergence, a damping factor is used between two consecutive iterations. In practice, this is achieved by affecting the gases' temperature at the end of each level, since this is the main parameter which is carried from one iteration to the other. A weighted average is calculated between each of the four values of the gases' exit temperatures and those obtained in the previous iteration (which had been stored in an additional variable) – equation (4.25).

$$T_{g\ out,level} = T_{g\ out,level} * (1 - dp) + T'_{g\ out,level} * dp \tag{4.25}$$

Where: $T_{g\ out,level}$ [K] is the gases' temperature at the end of each level; $T'_{g\ out,level}$ [K] is the gases' temperature at the end of each level, calculated in the previous iteration; dp is the damping factor.

This damping ensures that no abrupt variations occur in two consecutive iterations which may slow down the convergence process but avoids numerical instability problems.

As mentioned before, in order to simplify the model's construction, the fluid's temperature at the exit of the evaporator was considered the input variable (some value, even if arbitrary, must be specified for each simulation). This means that one of the model's outputs would be the fluid's temperature at the entry of the evaporator.

Naturally, this is not realistic since the real input will be the fluid's initial temperature and not its final. Therefore, an additional iterative cycle was created – one that encompasses the previously mentioned cycle, only leaving out the geometric calculations (since these are performed right at the beginning and are fixed throughout all simulations).

Once the model has converged and provided an accurate result for the fluid's temperature at the beginning of the evaporator, its enthalpy is compared to the enthalpy the fluid would have if it were at the "real" temperature at which it actually enters the evaporator– one of the model's inputs. This difference is stored in a control variable named *dif*, as seen on equation (4.26).

$$dif = H_{fluid,final} - H_{fluid,entry} \tag{4.26}$$

Where: dif [J/kg], given by equation (4.26), is a control variable for this new external cycle; $H_{fluid,final}$ [J/kg] is the fluid's enthalpy at the temperature of the beginning of the evaporator, calculated by the simulation; $H_{fluid,entry}$ [J/kg] is the fluid's enthalpy at the actual temperature the fluid will enter the evaporator (input variable).

After this, another iteration will begin where the fluid's enthalpy on CV no 1 is "corrected" by this variable, as shown by equation (4.27).

$$H_{fluid\ in,i=1} = H_{fluid\ in,i=1} - dif \quad \text{[J/kg]} \tag{4.27}$$

After the simulation has converged and produced a new value for the fluid's temperature at the entry of the evaporator, a new value for *dif* will be calculated and the cycle will repeat itself until this variable, once again, reaches below a desired value. The reason why the enthalpy is used as a comparison instead of the temperature is to enable the iterative process to converge even if the fluid is leaving the evaporator in a two-phase flow (even though the ORC is not supposed to run this way).

Once this cycle ends, the simulation is considered complete with the fluid's final temperature now being an output variable. Annex B (Figure B. 1) contains a flow-chart which demonstrates the basic operating principles of the model, namely the aforementioned iterative cycles.

Having described all three models, their results may now be analysed and evaluated. The next Chapter will perform a parametric analysis of the outputs produced by these models and attempt to explain the physical phenomena behind the behaviour of a series of important parameters.

5. ANALYSIS OF RESULTS

In this chapter, an analysis will be performed on each of the previously described models' main results. Additionally, a series of small extra calculations which were performed on both the Post-Heater and the Evaporator's models will be explained and its results discussed as well.

5.1. Combustion Model's Results

Since the natural gas burner is the first component to be modelled, its results will be of great importance for the following models. Among these outputs, those with the largest influence on the heat transfer on the two heat exchangers will be the flame temperature and the gases' mass flow rate.

Taking this into account, the behaviour of these parameters and the way they relate to each other will now be analysed starting by the mass flow rate, plotted on a graph on Figure 5.1.

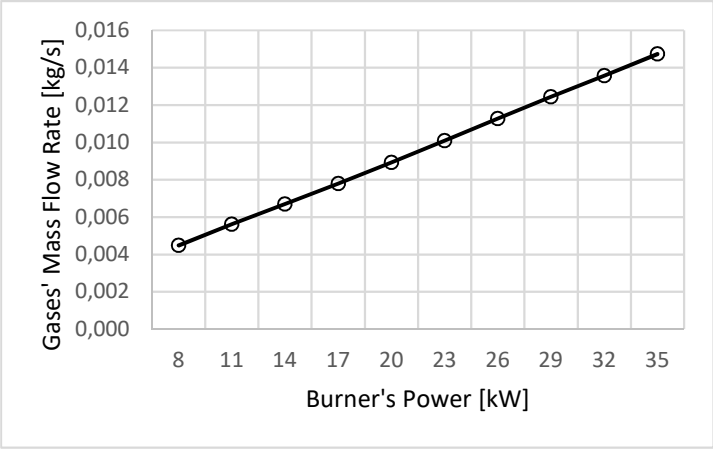

Figure 5.1. Combustion gases' mass flow rate as a function of the burner's power output.

As it can be seen, the combustion gases' mass flow rate follows a nearly perfect linear trend when plotted as a function of the burner's power output. This could be considered an interesting result as the excess of air is not constant along the burner's power

range, as seen on the graph from Figure 2.1.The flame temperature's behaviour, however, is clearly influenced by the excess of air, as demonstrated by Figure 5.2.

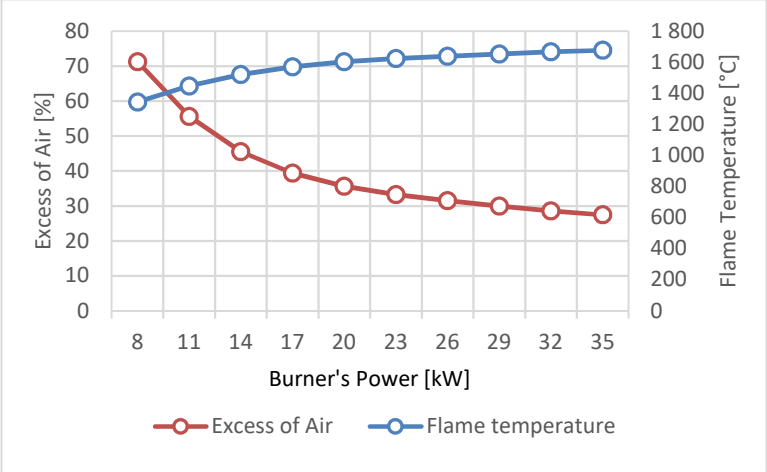

Figure 5.2. Flame temperature and excess of air as a function of the burner's power output.

The connection between the excess of air and the flame temperature can be further evidenced by plotting the second as a function of the first, as shown on as seen on Figure 5.3.

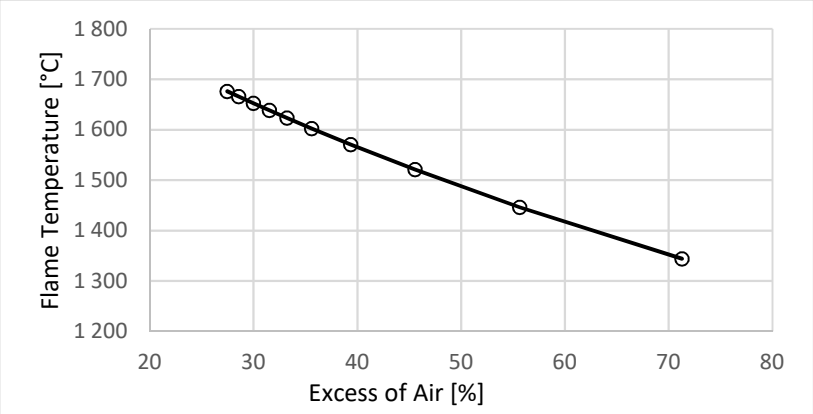

Figure 5.3. Flame temperature as a function of the excess of air.

By adapting a trend line to the to this graph on *Excel*, it appears that the relation between these two parameters is, in fact, quite linear. Indeed, it is known that the maximum combustion flame temperature is reached when the air-fuel mixture is rich which explains why this value is higher for lower levels of excess of air. This relation may prove to be quite important when attempting to control the fluid's maximum boundary layer temperature since, on the particular burner used, the excess of air can be manually adjusted.

5.2. Extra Calculations

In addition to the main objectives of the modelling performed on these three ORC components (Burner, Post-Heater and Evaporator), there are some small behavioural characteristics which are worth simulating as well (whether it's for safety reasons or simply to have a greater understanding of the way the cycle will work as a whole).

Taking this into account, three additional calculations will be described in this section and their respective results analysed.

5.2.1. Fin Tip Temperature

For safety reasons (as well as a proper material preservation), it is convenient to know the maximum temperature the fins will reach, which will occur on their tips.

In order to achieve this, the method presented on the "*Heat Transfer From Extended Surfaces*" section, from [10], was adopted. Here, the fin's temperature at any given point is determined by equation (5.1) - valid for annular fins of rectangular profile:

$$\frac{\theta}{\theta_b} = \frac{I_0(mf * r) * K_1(mf * r_2) + K_0(mf * r) * I_1(mf * r_2)}{I_0(mf * r_1) * K_1(mf * r_2) + K_0(mf * r_1) * I_1(mf * r_2)} \quad (5.1)$$

Where: θ [K] = temperature difference between the surroundings and the desired point; θ_b[K] = temperature difference between the surroundings and the fin's base; I_0 = zero-order modified Bessel function of the first kind; K_0 = zero-order modified Bessel function of the second kind; I_1 = first order modified Bessel function of the first kind; K_1 = first order modified Bessel function of the second kind; r_1 [m] = fin's radius, at its base; r_2 [m] = fin's radius at its tip, corrected in order to include the heat transfer in that area; r [m] = fin's radius at the desired point;

- $mf = \sqrt{\frac{2h}{k*t}}\ [m^{-1}]$ (5.2)

$h\ [W/m^2K]$ = external convection coefficient (on the gas' side); $K\ [W/m.K]$ = fin material's thermal conductivity (copper); t [m] = fin's thickness.

The *Bessel* Functions, which can be found in a series of tables, were inserted in the models via mathematical functions (polynomial of degree six for the first kind and exponential for the second kind).

Since only the maximum temperature is needed, the point at which the fin's temperature is calculated will always be its tip ($r = r_{fin\ tip}$), as seen in equation (5.3):

$$T_{fin,tip} = T_{in,g} - \frac{\theta}{\theta_b} * (T_{in,g} - T_{tube\ ext}) \tag{5.3}$$

Where: $T_{fin,tip}$ [K] is the temperature of the fin's tip; $T_{in,g}$ [K] is the surrounding gas' maximum temperature, which happens at the entry of each level (since this is mainly a safety calculation); $T_{tube\ ext}$ [K] is the tube's exterior temperature.

While the Bessel functions are calculated for each level in the evaporator's case and just once for the Post-Heater, the value of $T_{t\ ext}$ is specific of each control volume, which results in two values of $T_{fin\ tip}$ for the Post-Heater and *Nc*14* for the Evaporator.

The results for the maximum fin tip temperature (as well as the maximum tube's exterior temperature) for the Post-Heater and the Evaporator can be seen, respectively, on Table 5.1 and Table 5.2 for three different power levels.

Table 5.1. Maximum fin tip and tube's exterior temperature on the Post-Heater.

Post-Heater			
Burner Power [kW]	37	20	8
Maximum Fin Tip Temperature [°C]	252.6	224,8	190,6
Maximum Tube's Exterior Temperature [°C]	238,3	215,7	186,2

Table 5.2. Maximum fin tip and tube's exterior temperature on the Evaporator.

Evaporator			
Burner Power [kW]	37	20	8
Maximum Fin Tip Temperature [°C]	612,0	482,3	363,2
Maximum Tube's Exterior Temperature [°C]	569,2	458,2	356,5

The simulations at different power levels were performed according to the parameters defined on Table 5.3.

As it may be observed, the maximum temperature difference between the fin's base and its tip is 43 °C. This happens on the evaporator (where the fins are longer) and at the maximum power level (maximum flame temperature and gases' mass flow rate). It is worth noticing that this result comes from the fact that the fins' efficiencies is extremely

high (due to their relatively short length and highly conductive material) which means that mean fin temperature is relatively close to that of its base. Since the maximum temperature reached (612°C) is within the fins' operating temperature (see [12]), the simulations suggest that this parameter should raise no problem during the ORC's operation. Additionally, the real value should be even lower due to the conduction along the fin's perimeter, which was not considered.

Table 5.3. Simulation parameters for three different power levels.

Burner Power [kW]	37	20	8
Excess of Air [%]	27,2	35,6	71,3
Flame Temperature [°C]	1680	1603	1344
Gases' Mass Flow Rate [kg/s]	0,0155	0,0089	0,0045
Water Mass Flow Rate on the Post-Heater [kg/s]	0,080	0,060	0,033
Water's Outlet Temperature on the Post-Heater [°C]	85	85	85
Fluid's Mass Flow Rate on the Evaporator [kg/s]	0,090	0,045	0,015
Fluid's Outlet Temperature on the Evaporator [°C]	108	108	108

5.2.2. Pressure Drop in the Gas Flow

The main reason why this parameter is worth calculating is to know whether some dedicated gas extraction system is needed or if the burner's own ventilation system is sufficient to ensure a proper exhaust gas flow.

This calculation relies on one equation only (5.4) (see [10], "*Compact Heat Exchangers"* section). The result is the pressure drop (Δp) associated with a gas flow across finned-tube banks.

$$\Delta p = \frac{G^2 * v_i}{2}\left[(1+\sigma^2) * \left(\frac{v_{out}}{v_{in}} - 1\right) + f * \frac{A}{A_{ff}} * \frac{v_m}{v_{in}}\right] \qquad [Pa] \tag{5.4}$$

Where: G $[kg/m^2 s]$ is the gas' maximum mass velocity; v_{in} $[m^3/kg]$ is the gas' initial specific volume; v_{out} $[m^3/kg]$ is the gas' final specific volume; v_m $[m^3/kg]$ is the gas' mean specific volume; σ is the area ratio; f is the friction factor, measured from a graph [10] (as a function of the Reynolds number); A $[m^2]$ is the total heat transfer area; A_{ff} $[m^2]$ is the free-flow area.

The pressure drop for the three same simulation conditions as those used in section 5.2.1 are found, for both the whole assembly, on Table 5.4.

Table 5.4. Pressure drop in the gas flow for three different power levels.

Burner Power [kW]	37	20	8
Pressure Drop in the Gas Flow [Pa]	7,25	2,27	0,578

After analysing this table one can conclude that, according to the simulations, the pressure drop on the gas flow across the two exchangers is extremely low (less than 8 Pa in the most extreme case) meaning that this phenomenon may not be relevant.

5.2.3. Pressure Drop in the Working Fluid

In order to properly select a suitable pump for the installation (capable of sending the desired flow of WF through the circuit), it is important to know the pressure drop the fluid will suffer as it travels through the evaporator.

The fluid's pressure drop may be split in three main components:

- Pressure drop due to friction (continuous as the fluids travels through the evaporator's pipes);
- Local pressure drops due to the existence of components (such as valves, elbows, U-turns, etc);
- Pressure drop due to the height elevation inside the evaporator (hydrostatic).

The continuous pressure losses are calculated individually for each control volume and rely on the formula given by equation (5.5):

$$\Delta p = hf * \rho * g \quad [Pa] \tag{5.5}$$

With the pressure drop in terms of fluid column being given by equation (5.6):

$$hf = f * \frac{\Delta L}{D_{int}} * \frac{v^2}{2g} \qquad [m] \tag{5.6}$$

Where: Δp [Pa] is the pressure drop; ρ $[kg/m^3]$ is the fluid's density; g $[m/s^2]$ is the gravitational acceleration; ΔL [m] is the length of each CV; v [m/s] is the fluid's velocity; f is the *Darcy* coefficient of friction, given by equation (5.7):

$$\frac{1}{\sqrt{\mathrm{f}}} = -1.8 * \log\left[\frac{6.9}{Re} + \left(\frac{\varepsilon r}{3.7}\right)^{1.11}\right] \tag{5.7}$$

For the local pressure drops all the turns between each evaporator tube were considered as well as its entry and exit (which correspond to a cross-section enlargement and contraction, respectively). The general expression is shown on equation (5.8):

$$\Delta p = kp * \frac{1}{2} * \rho * v^2 \quad [Pa] \tag{5.8}$$

Where *kp* is a pressure drop factor specific for each type of component. Typical values of *kp* can be found in the form of graphics and/or tables (see [13], [14]).

The pressure drop due to the height difference between the evaporator's entry and exit Δz [m] can be calculated by equation (5.9):

$$\Delta p = \Delta z * \rho * \mathrm{g} \tag{5.9}$$

After all the parcels have been calculated, they are simply added resulting in the total pressure drop across the evaporator.

Once again, results for three different power levels are shown in Table 5.5.

Table 5.5. Pressure drop in the Organic Fluid for three power levels.

Burner Power [kW]	37	20	8
Pressure Drop on the Organic Fluid [kPa]	5,02	2,43	1,75

As expected, the pressure drop is higher when the fluid's mass flow rate is higher (resulting in an increased velocity). As interesting analysis may be looking at the three pressure drop "parcels" separately, as demonstrated by the graph on Figure 5.4.

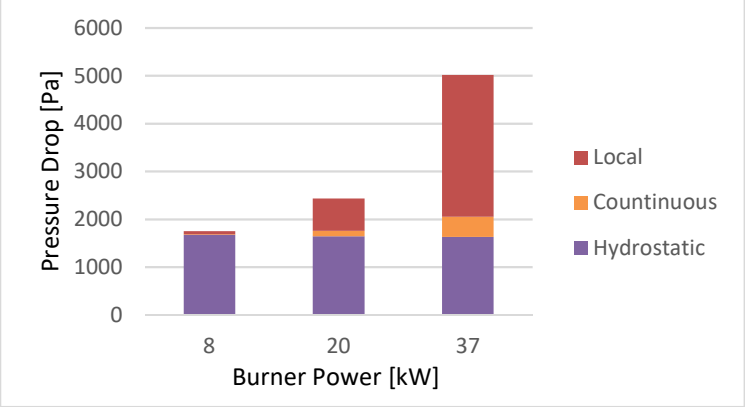

Figure 5.4. Weight of each type of pressure drop on the organic fluid.

Naturally, the hydrostatic pressure difference remains unchanged throughout different power levels while the other two increase with it (result of the fluid's increasing mass flow rate and, therefore, velocity). It is worth mentioning, however, that when considering the whole circuit, this parcel (which has a large weight on the overall pressure drop) will be 0 since it is a closed loop.

As one may assume, this pressure loss is not constant throughout the evaporator. Figure 5.5 shows the evolution of the WF's pressure loss as it travels through the evaporator for a burner power of 37 kW (the hydrostatic pressure difference is not included). The graph's abscissa axis represents the number of tubes in the Evaporator (14 in total) and the corresponding position according to a linear coordinate L [m], with $L=0$ being the point at which the fluid enters the Evaporator. The dotted lines mark the separation between each level of tubes.

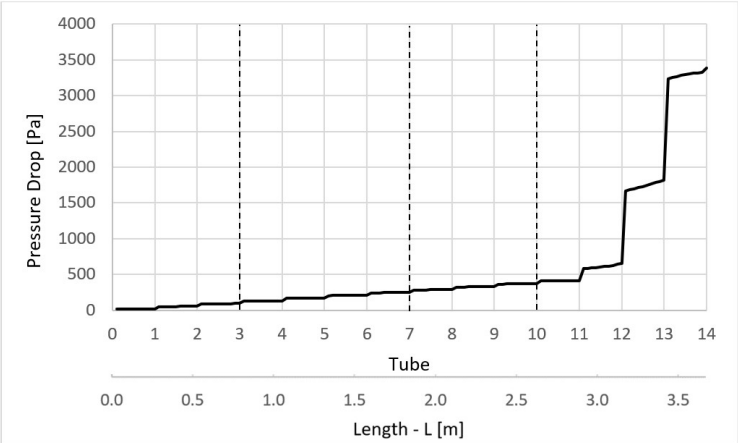

Figure 5.5. Continuous and local pressure losses inside the evaporator.

As it can be observed, the local pressure losses have the largest contribution (conclusion which could also be made by analysing Figure 5.4). This happens at the evaporator's entry and exit as well as between each of its tubes (where U-turns are located). In addition, it is clear that both parcels radically increase after tube 11. This is the point where the WF enters two-phase flow, for this power level (as will be demonstrated on Section 5.3). This increase is due to the fact that, as the fluid turns into vapor, its velocity rises significantly resulting in larger pressure losses (both due to friction inside the tubes as well as specific components).

5.3. Post-Heater & Evaporator Model's Results

This section contains an analysis of some of the results provided by the Post-Heater and Evaporator's models. The choice was made not to separate the two since both describe physical phenomena of heat transfer from a gas to a fluid and both the components simulated are no more than heat exchangers assembled on top of each other.

A series of simulations were carried out for different power levels. However, with the exception of a few parameters, it would be redundant to present the results for all of them since the variables in main focus have a similar behaviour in all scenarios.

Therefore, the results presented in the following figures were obtained under the simulation conditions described on Table 5.3 with a burner power of 37 kW, starting by the temperature of the combustion gases as they travel through the exchangers - Figure 5.6.

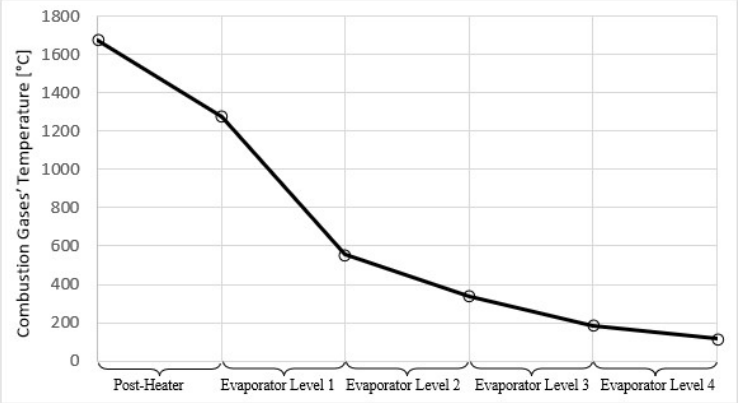

Figure 5.6. Combustion Gases' temperature variation.

As mentioned on Chapters 3 and 4, heat transfer by radiation is considered in all levels of the evaporator as well as the post-heater. However, its weight on the total heat transfer is not constant, as clearly demonstrated by Figure 5.7.

The graphs that will then follow show the behaviour of several parameters considered relevant for the characterization of the evaporator:

- Internal heat transfer coefficient h_{fluid} - Figure 5.8;
- Power transferred per CV (for a total of 10 CVs per tube) Q_i - Figure 5.9;
- Tube's internal temperature $T_{tube\ int}$ - Figure 5.10;
- Working Fluid's temperature T_{fluid} - Figure 5.11.

The reason why these same results are not provided for the Post-Heater is that, with only one heat exchanger level, two CVs and a relatively low temperature change in the water, all these variables remain practically constant with the exception of the water temperature which increases almost linearly.

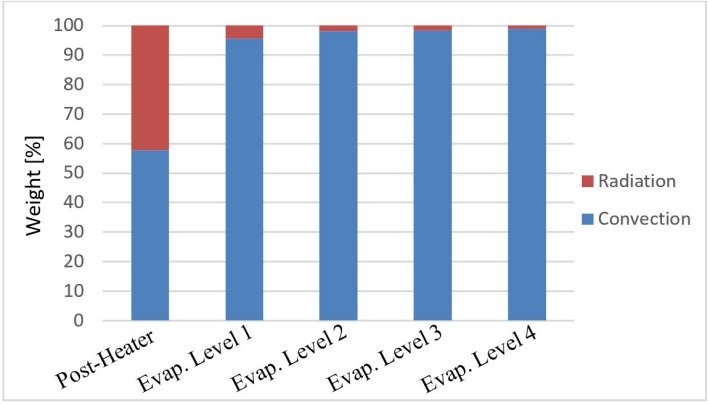

Figure 5.7. Weight of the heat transfer by convection and radiation on each level.

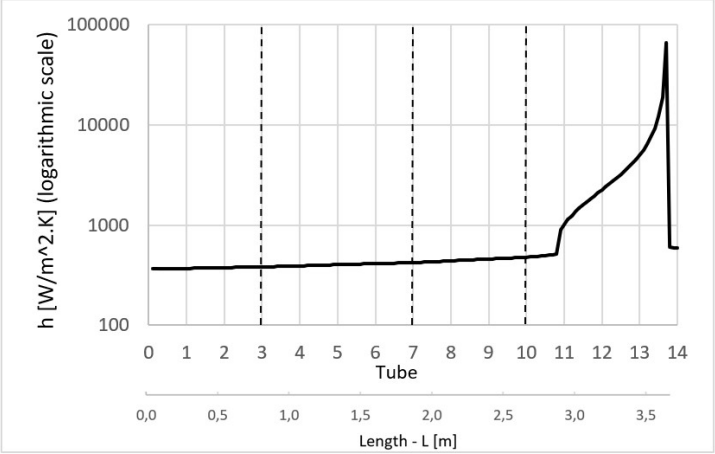

Figure 5.8. Internal Heat Transfer coefficient

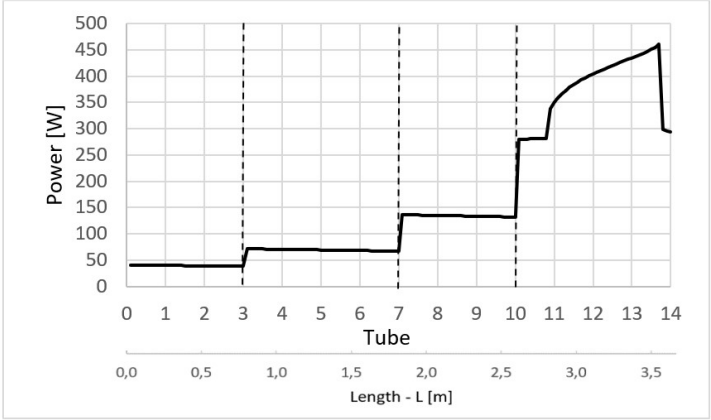

Figure 5.9. Power Transferred per CV.

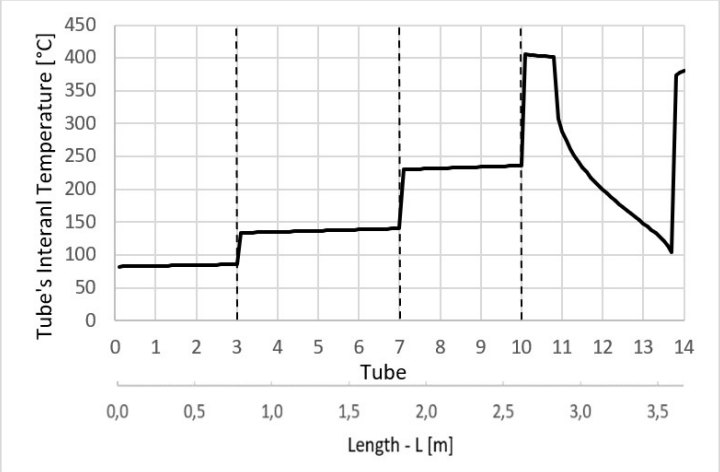

Figure 5.10. Tube's internal temperature.

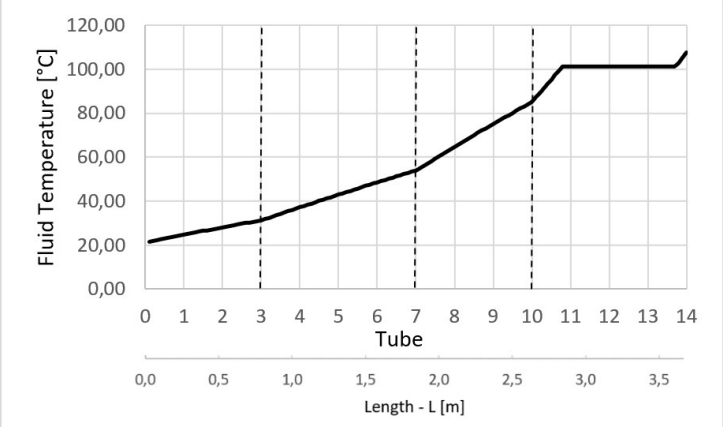

Figure 5.11. Working fluid's temperature.

Starting by Figure 5.6, one can see that no particularly surprising results are to be found. Since this graph includes both the post-heater and the evaporator, it is only natural that there are two distinct behaviours/trends as the gases travel through each component. It is also not surprising that as the gases' temperature drops, the heat transfer also decreases resulting in a lower temperature loss rate.

The results shown on Figure 5.7 were also predictable since not only is the gas volume (on eq. (3.10)) much larger on the post-heater than on each level of the evaporator but also the area of heat transfer is considerably smaller (due to fewer and shorter fins). This leads to a Mean Beam Length which, on the evaporator, is smaller by approx. one order of magnitude (compared to the post-heater). In addition, as the gas temperature decreases from one level to the other, the influence of the radiation is also reduced.

Moving on to Figure 5.8, it can be seen that the internal heat transfer coefficient remains fairly steady until close to tube 11. This is the point where the fluid enters the two-phase flow. This type of flow is typically characterized by extremely high values of h_{fluid} which may increase by approximately one order of magnitude compared to the sub-cooled region [10]. In fact, the increase is so high that a logarithmic scale had to be used for the ordinate axis in order to facilitate the interpretation of the graph. This parameter reaches its peak as the fluid enters *Annular Flow* (the liquid forms a film next to the tube wall as the vapor moves at great speed through its middle), followed by the *Mist Regime* (small droplets of liquid which travel in the core of the tube) [10]. The heat transfer coefficient then suddenly drops as the fluid returns to a single-phase flow – now vapour.

As mentioned on Chapter 4, the value of $\frac{1}{Xtt}$ (a parameter necessary for the calculation of h_{flu}) may go beyond its interval of applicability, resulting in unrealistically high values of h_{fluid} for one of two CVs. Nevertheless, and as previously mentioned, since the thermal resistance on the gas' side is, for the two-phase flow, much higher than on the fluid's side, this will not have a great effect on the value of Q_i, as see on Figure 5.9. It may initially look like the power transferred per CV follows a similar trend to h_{fluid} (except for the "steps" as the fluid changes level and, therefore, is subjected to much higher gas temperatures resulting in an increased heat transfer). However, one must not forget that this graph (Figure 5.9) is not presented with a logarithmic scale. Indeed, while the value of h_{fluid} rises more than one order of magnitude in the two-phase region, Q_i only increases by approx. 50%. More precisely, the value of h_{fluid} increases by over 3 times on the CV where $\frac{1}{Xtt}$ is beyond its limits while Q_i only grows by 1,2% (both compared to their corresponding values on the previous CV).

The parameter where h_{fluid} has a visible effect is on the tube's internal temperature (Figure 5.10). On the first three levels, this parameter rises at a constant yet slow place as we move through the Evaporator with clear "jumps" appearing at the separation of each level. On the last level, however, there is a great drop in this temperature during the two-phase flow region followed by an abrupt rise back to its "normal" single-phase value, on the last tube. This is due to the increase of h_{fluid} and, therefore, a decrease on the internal thermal resistance. This is also where one of the model's limitations shows its effects. Indeed, it is not realistic that such an enormous temperature variation occurs in one single

tube whose length is only 26,4 cm. This happens due to the fact that no heat conduction along the tubes' walls was considered due to the high complexity its integration would involve. In reality, due to this phenomenon, this temperature variation (even if as large) would be more gradual and not as abrupt. Nevertheless, according to this simulation, the tube's internal temperature may rise to significantly high values due to the fact that the incorporation of extended surfaces brings the thermal resistance on the gas' side close to that on the fluid's side. This combined with the fact that the first level of the evaporator (tubes 10-14) is exposed to extremely high gas' temperatures results in a potentially dangerous boundary layer temperatures of the organic fluid (dangerous since the fluid may be subjected to thermal degradation). Nonetheless, it was observed that, as the power is set to gradually lower levels (such as the other two shown on Table 5.3) the maximum temperature on the tubes' internal wall also deceases (while the overall trend seen on Figure 5.10 is always the same). This is verified for any given power within the burner's range as long as the WF's flow rate is adjusted in order to maintain similar inlet and outlet fluid temperatures.

Finally, the behaviour of the fluid's mean temperature does not show anything unexpected. Its rise is constant for each of the first three levels with visible changes in the first derivative as the fluid moves up a level. On the last one, the fluid's entire evaporation occurs (at a constant temperature) as well as a small degree of superheating (approx. 6 °C).

Having analysed these graphs and provided some explanations for the phenomena observed, it would now be interesting to visualize the effect h_{fluid} on the radial temperature distribution. That is to say, the way the temperature changes as we move from the inside of the tubes until their exterior. This can be seen on Figure 5.12 for two distinct cases:

- Two-phase flow (x = 0,69) - h_{fluid} is extremely high;
- Single-phase flow (vapor superheated by 1 °C) - h_{fluid} is much lower.

*Note: the gas temperature presented is the mean temperature on the 1st level.

These graphs make it easy to visualize how the internal convection coefficient (which is the only parameter that changes significantly between the two graphs as the fluid's temperature difference is only around 1 °C) affects the temperature distribution. On (a) h_{fluid} is extremely high and, therefore, the internal thermal resistance is significantly lower than the external which brings the tube's temperature much closer to the fluid's. On (b),

however, the internal thermal resistance goes up and, due to the fact that the tubes have fins on their exterior (they were not represented on the graph for the sake of simplicity), both thermal resistances come close to each other which results in a tube temperature which is somewhat between the fluid's and the gas' temperature.

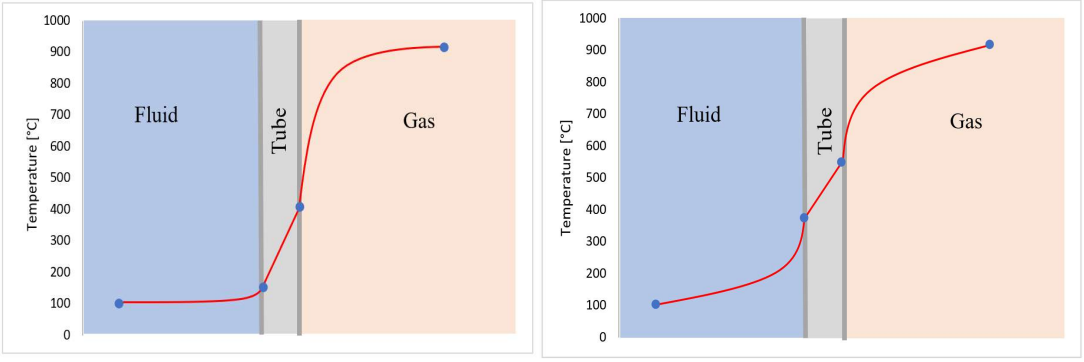

(a) (b)

Figure 5.12. Radial temperature distribution for two-phase flow (a) and superheated vapor (b).

It was previously stated that most parameters would remain unchanged throughout the simulations at different power levels. One that does not, however, is the distribution of the heat transferred in the Post-Heater and Evaporator. The graph on Figure 5.13 shows the portion of power which is transferred on each of the two components as well as that which is lost (both in the chimney and to the exterior of the Evaporator). The results for a burner power of 8, 20 and 37 kW were obtained according to the conditions established on Table 5.3 with the additional two (14 and 28 kW) being performed so that the both the working fluid and the water suffered the same temperature increase as in the three previous ones (this was achieved by adjusting their mass flow rate).

It can be observed that, for lower power levels, the portion of power transferred in the Post-Heater is much larger (going from nearly the same as the Evaporator for 8 kW to 2,5 times less for 37 kW). In fact, this is not a big surprise. If the Post-Heater is seen as merely another level of the evaporator, it is expected that, as the power increases, the first level is no longer capable of absorbing the same amount of power (relatively speaking) since this is limited by a wide range of parameters (such as the tube's conductivity, internal and external heat transfer coefficients, etc). Therefore, for higher power levels, there will be more energy left to absorb from the flue gases after these have gone through the first level. This is supported by the fact that, in the Evaporator alone, the power distribution through each level

does become more even as the burner's power rises. For 8 kW around 76% of the total power transfer in the Evaporator happens in the first level while for 37 kW this value drops to 65%.

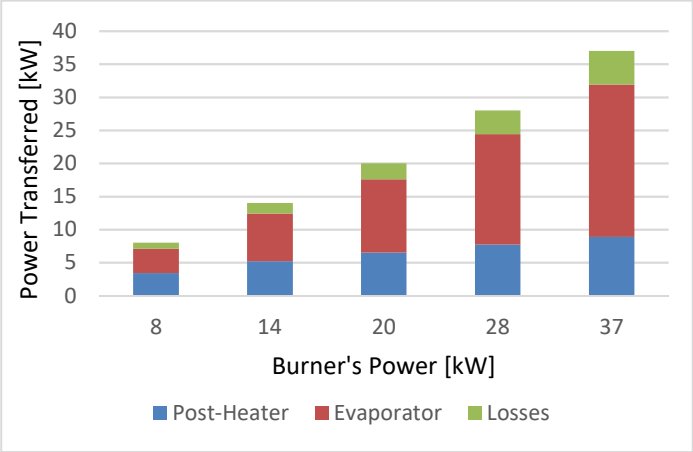

Figure 5.13. Power distribution between the two components (including losses).

Knowing the power supplied by the burner and the portion transferred on each component, the thermal efficiency of this part of the circuit can be calculated. The results for the same power levels as in Figure 5.13 are shown on Figure 5.14.

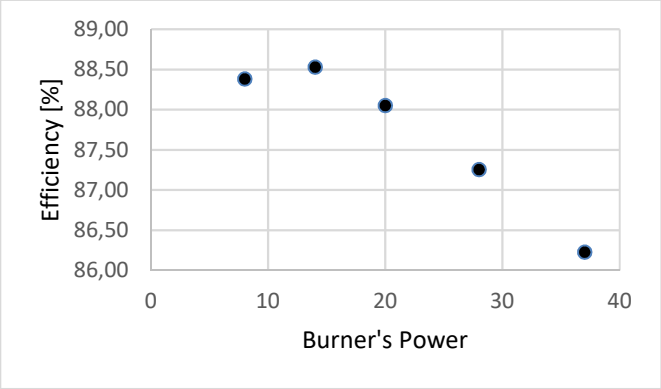

Figure 5.14. Efficiency of the Burner, Post-Heater and Evaporator assembly.

As it can be seen, the variation of this parameter for the whole power range of the burner is around 2,5% with no clear trend being detected.

Now that a series of important outputs of each model have been presented and analysed, the next chapter will proceed to describe the characteristics of the test rig used to perform the experimental analysis as well as the way these tests were performed.

6. EXPERIMENTAL ANALYSIS

In order to verify and validate the results provided by the model it is essential that the Post-Heater and Evaporator are tested as part of an actual ORC. Indeed, the mathematical model developed intends to simulate a series of physical phenomena meaning that theoretical results alone don't possess enough strength unless supported by experimental data. Furthermore, carrying out these tests allows investigators to cover a series of smaller physical phenomena which, for one reason or another, were not always included in the models' construction.

To achieve this, a prototype *Organic Rankine Cycle* was built in the facilities of the Department of Mechanical Engineering (*Departamento de Engenharia Mecânica* – DEM) of the University of Coimbra – UC. The following section will consist of a description of this installation.

6.1. Test Rig Description

As it can be seen on Figure 1.1, the installation consists of a series of components typically found in *Rankine Cycles*, namely:

- A pump;
- A working fluid evaporator;
- An expander;
- A condenser.

However, a few important differences can be seen on this particular prototype. Firstly, and as previously mentioned, the ORC evaporator is not placed immediately after the burner but after the Post-Heater. As it can be seen in the complete scheme of the circuit (Figure E. 1, Annex E), the water initially flows through the condenser (removing thermal energy from the organic fluid and heating up in the process) after which it is fed to the Post-Heater where its temperature will be raised even further, leading to a reduction in the combustion gases' temperature.

Secondly, the working fluid's expansion is not performed in a turbine (which would be used to power an electric generator) but instead in a throttling valve. This choice was made due to the fact that the main objective of this installation is to test the ORC evaporator since most of the other components are considered to be "off-the-shelf", that is to say, they do not need great further development for this specific purpose. The evaporator, however, cannot be found on sale and was built specifically for this ORC. Replacing the turbine by a throttling/expansion valve does not affect the evaporator's behaviour. The only difference being that the condenser must be chosen so that it can transfer the additional energy which would otherwise be absorbed by the turbine, since the fluid's expansion is now isenthalpic and not isentropic.

Since this thesis work focuses on the modelling of the evaporator section only (NG Burner, Post-Heater and Evaporator itself), a description of the instrumentation installed in this section of the prototype will now follow.

A series of temperature sensors (thermocouples) are placed along the gas, water and working fluid's circuit as demonstrated by Figure 6.1 and Figure 6.2.

Additionally, sensors no **1** and **2.0** are located at the working fluid's entry and exit of the evaporator, respectively. Sensors no **6.0** and **7** are located in the water circuit, before and after the Post-Heater (see Figure E. 1).

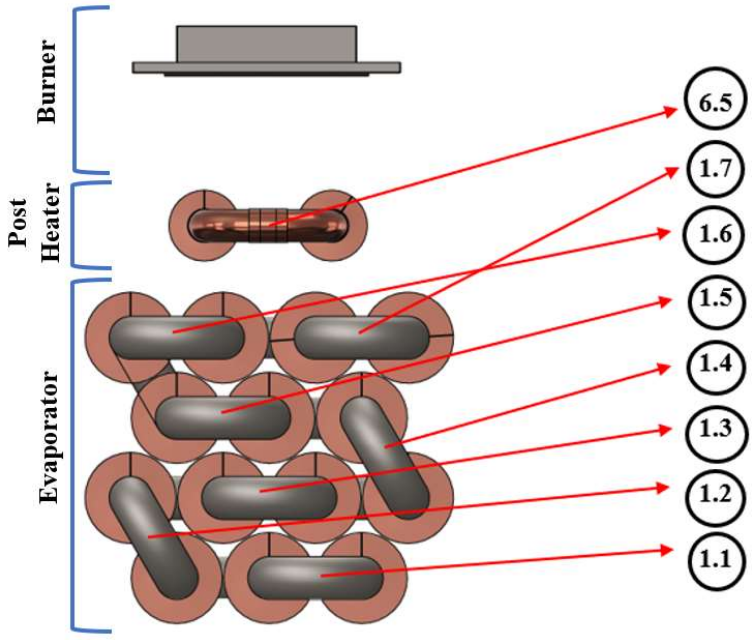

Figure 6.1. Location of the fluid and water thermocouples on the Evaporator and Post-Heater.

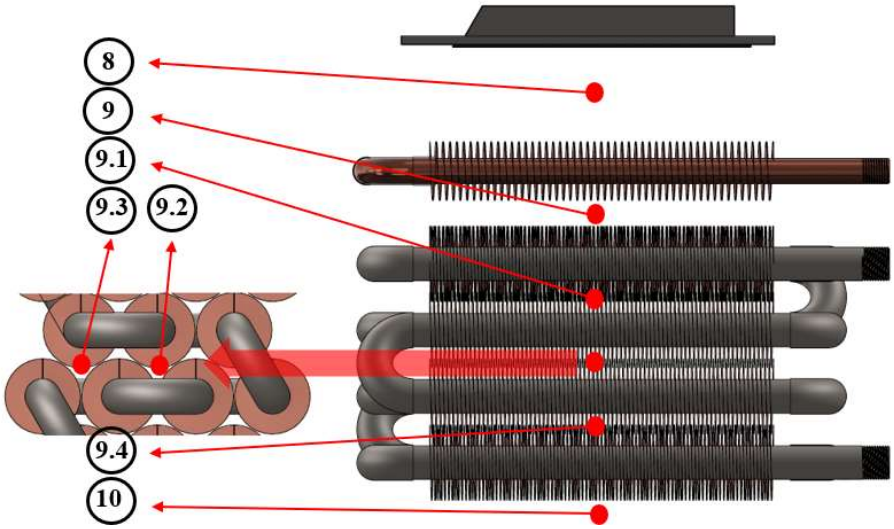

Figure 6.2. Location of the gas thermocouples on the Evaporator and Post-Heater.

On Table 6.1, the main characteristics of each thermocouple used can be found. All of the sensors which measure the WF's and water's temperature (with the exception of **2.0**) have a contact probe. This means that the actual measured temperature is that of the tube's exterior (on the turns), where the thermocouple's tips are attached to. This area is outside the gas flow zone and is externally insulated. The gas' temperature sensors have regular probes which are inserted inside of the evaporator. Sensor **2.0**'s probe is in placed direct contact with the WF's flow.

Table 6.1. Thermocouples' characteristics. t = Measured Temperature

Sensor no.	Type	Range [°C]	Accuracy
1 – 2.0; 6.0 – 7	T	- 40 to 300	0,0075 |t| or 1°C
10	T	-40 to 300	0,0075 |t| or 1°C
9 – 9.4	K	-40 to 1100	0,0075 |t| or 2,5°C
8	R	0 to 1600	0,0025 |t| or 1,5°C

Another key parameter for the validation of the model is the pressure at which the fluid flows through the evaporator. This is measured by a pressure sensor P1 (located after the pump) and P2 (after the evaporator). Table 6.2 contains the characteristics of these

two sensors as well as two additional ones found in the installation: P3 – located after the expansion valve; P4 – located between the condenser and the pump.

Table 6.2. Pressure sensor's characteristics. F.S = Full Scale

Position	Type	Reading	Range [bar]	Accuracy	Max. Temperature [°C]
1,2	Diaphragm	Relative	0 - 25	0,25% F.S	120
3	Diaphragm	Relative	0 - 10	0,25% F.S	120
4	Diaphragm	Relative	-1 - 9	0,25% F.S	120

In order to determine the mass flow rate of both the water and the organic fluid a series of flowmeters are required. In the complete installation only two of these can be found and both in the water circuit – one after the condenser and another just before the Post-Heater. This is due to the fact that, thanks to a series of valves and a T connection, not all of the water which flows through the condenser has to travel through the Post-Heater meaning that two readings are required. The characteristics of both flowmeters (which are identical) can be found on Table 6.3.

Table 6.3. Flowmeter's characteristics.

Type	Range (l/min)	Accuracy	Max. Temperature [°C]	Max. Pressure [bar]	Pressure Drop [bar]
Pulse	1 - 25	2%	70	20	0,1

The original solution to obtain the WF's flow rate was a *Coriolis* mass flow sensor. However, due to a series of conditioning factors, it could not be installed in time for the tests. Therefore, the WF's flow rate was determined indirectly. This is achieved by making an energy balance in the condenser. The inlet and outlet temperatures for both fluids are known as well as the water's mass flow rate. By assuming a specific value for the condenser's efficiency, the mass flow rate of the WF can be determined, as seen on equation (6.1):

$$\dot{m}_{water} * cp_{water} * \Delta T_{water,cond} = \eta * \dot{m}_{fluid} * \Delta H_{fluid,cond} \quad (6.1)$$

Where: $\Delta T_{water,cond}$ [K] is the temperature variation in the water (in the condenser); η is the condenser's efficiency; $\Delta H_{fluid,cond}$ [J/kg] is the fluid's enthalpy variation in the condenser.

Concerning the gases, there are two devices needed to obtain the necessary inputs for the model: the Gas Meter (to measure the consumption of NG) and the Gas analyser (to obtain the composition of the combustion gases). Their respective characteristics can be found on Table 6.4 and Table 6.5.

Table 6.4. Gas Meter's characteristics.

Type	Range [m^3/h]	Accuracy	Op. Temperature [°C]	Max. Pressure [bar]
Diaphragm	0,04 - 6	1%	-25 - 55	0,5

Table 6.5. Gas analyser's measurement capabilities.

Sample Gas	Range	Accuracy [%]
Carbon Dioxide	0 – 20%	1
Carbon Monoxide	0 – 500 ppm & 0 – 5%	1
Hydrocarbons	0 – 1000 ppm	1
Oxygen	0 – 25%	1
Nitric Oxide	0 – 250 ppm	1

The Thermometer/Hygrometer is the last device relevant to the validation of the models, since it measures the air temperature and humidity (both of which are input variables of the combustion model).

Table 6.6. Thermometer/Hygrometer's characteristics.

Type	Temperature Range [°C]	Humidity Range [%]	Accuracy [%]
Analogue	-20 - 40	20 - 80	5

Having completed the overall description of the test rig used, the next section will focus on the experimental tests performed and the way these were conducted.

6.2. Experimental Tests

Using the ORC prototype installation, a series of experimental tests were carried out under a variety of different conditions (burner power, WF and water' mass flow rate) in order to validate the model in its entire range.

In an initial stage, the WF's superheating was maintained at around 5 °C while the burner's power output was gradually risen from approx. 10 kW to 30 kW. This was achieved by adjusting the pump's speed according to the supplied power. The water's mass flow rate (in these tests, equal on the condenser and post-heater) was maintained relatively constant throughout these tests by adjusting one of the needle valves in its circuit.

Once this range had been covered, the power was set to an intermediate level (around 17 kW) in order to carry out a few final experiments. The first of which consisted in raising the WF's flow rate until it left the evaporator in a two-phase flow instead of superheated vapor. This was followed by a test where its superheating level was raised up to around 10°C. Finally, the water's mass flow rate was lowered significantly and the WF's superheating set back to 5 °C.

The outputs were automatically saved in a series of files with the exception of the surround air conditions, gas analyser's outputs and NG's consumption which were registered manually. The aforementioned data which is automatically saved is recorded for every second of the test. For each individual trial, a period of approx. 10 minutes (after the system had stabilized) was analysed with an arithmetic mean being calculated out of all these individual points (for each desired output). This ensures that the results which will be compared with the model are representative of the condition the system reaches once it has stabilized and not the cause of a temporary change in one of the input variables (such as the water's flow rate, which cannot be controlled entirely due to the distribution system).

In the following chapter (section 2) the results of these tests will be compared to those provided by the model in order to verify its correct functioning as well as to explain a few differences which may arise. The increase in the water/WF's temperature (and, consequently, the power transferred in the Post-Heater/Evaporator) will be the main variables used to perform this validation since these are believed to me measured with greater accuracy than the gas' temperature, while performing the tests.

7. MODEL VALIDATION

7.1. Preliminary Validation

In an earlier stage of the elaboration of this thesis work, when the combustion and heat transfer models had just been completed, it was decided that a brief validation should be conducted in order to verify their overall correct functioning. Since the test rig described on Chapter 6 had not yet been completed (as its construction took place simultaneously with the development of the model), this could not be done with results from the actual ORC prototype.

Therefore, the outputs of the model were instead compared to a series of results obtained in an earlier stage, when testing the evaporator alone. This meant that, in this configuration, no Post-Heater was used as the NG Burner was assembled directly on the Evaporator. Since there was no complete installation at the time the tests took place, they were conducted with water flowing inside the Evaporator's tubes (in an open circuit).

The conditions under which these tests were performed have several implications in this "Preliminary Validation", namely:

- Since the fluid used was water and, with the mass flow rates tested, no evaporation occurred, these results may only verify the correlations used for a single-phase flow. Additionally, it can only be concluded if they are adequate (or not) for water and not for the organic fluid used in the complete ORC installation;
- Not only were the temperature sensors not placed exactly on the same locations as in the final test rig but also the accuracy of some of their measurements may be questionable, as will be discussed further ahead;
- None or little thermal insulation was used on this assembly which resulted in increased losses. Since the model developed does not account for such phenomenon (given that the Evaporator in the final test rig will be well insulated), they were manually inserted with the actual values of thermal losses measured in these tests being used;

- Finally, and as previously mentioned, no Post-Heater was used and, therefore, it may not be validated with these results alone (even though this test may indicate whether the methods used are adequate or not, since they do not differ much from the Evaporator, for single-phase flow).

The variable which will be evaluated here is the total power transferred in the Evaporator. In the tests performed, this was calculated using the total increase in the water temperature inside of the evaporator and its mass flow rate. This could also be determined by the gases' temperature change, but it was decided not to do so due to reduced accuracy of the temperature sensors used to measure this parameter. The model's outputs include both the power transferred and the evolution of the water temperature (as well as the gases'). As mentioned, the former was chosen to serve as a comparison. The power supplied by the burner was calculated, in these tests, using the consumption of NG and its composition, both of which are inputs of the combustion model. In addition to these inputs, the water temperature at the entry of the Evaporator was set equal to that of the tests (as well as its mass flow rate) with its outlet temperature being the output variable.

The comparisons were made for six different power levels of the burner, as shown on Table 7.1.

Table 7.1. Comparison of the Power Transferred to the water for the Model and Tests.

Burner Power [kW]	7,950	13,087	18,736	24,663	30,446	36,267
Power Transferred – Model [kW]	7,245	11,473	16,602	21,433	26,286	30,397
Power Transferred – Tests [kW]	7,446	12,010	17,420	22,560	27,780	32,110
Relative Error [%]	-2,687	-4,471	-4,696	-4,996	-5,378	-5,335

In order to have a perception of how the results of the tests compare to those of the model, Figure 7.1 and Figure 7.2 show graphs of the combustion gases and water temperature, respectively, for a burner power of 24,663 kW. The gases' temperature was measured at the beginning of the Evaporator and after each level while the water's was measured on 8 different points with 0 being the inlet and 7 the outlet.

As it can be seen, without any calibration factor (other than the thermal losses inserted in the model), the results do not differ greatly from each other with the maximum

relative error being -5,4%. This can partially be attributed to inaccuracies in the measurements. Taking the case of the combustion gases, it is clear that the first temperature values (just before the Evaporator) are quite different. This could be a result of thermal losses on the thermocouple itself. Indeed, the one used on this point was type R, with the characteristics seen on Table 6.1. It is significantly larger and with a bigger surface area than the remaining ones which could result in the reading being not the actual temperature of the gases but of the thermocouple tip itself, which is achieved when heat transfer balance (in radiation, convection and conduction) is reached.

As to the water temperature measured on point 6, there may have been some kind of malfunction of the thermocouple since not only was this behaviour verified in all power levels but the resulting temperature profile obtained on these tests (on this particular location) did not make much sense, physically speaking.

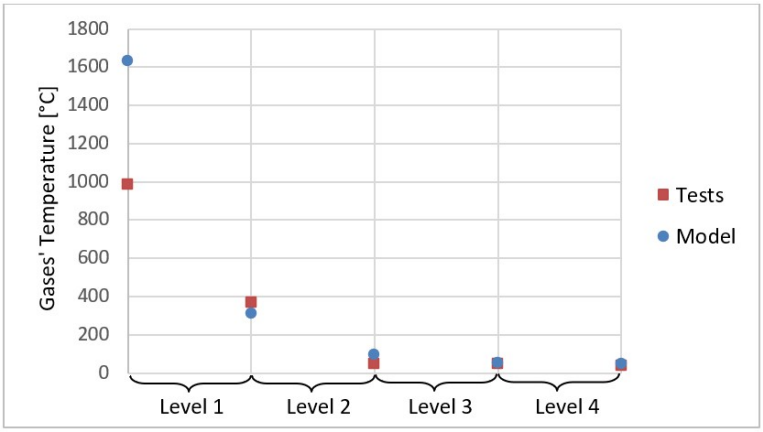

Figure 7.1. Gases' temperature results from the tests and model.

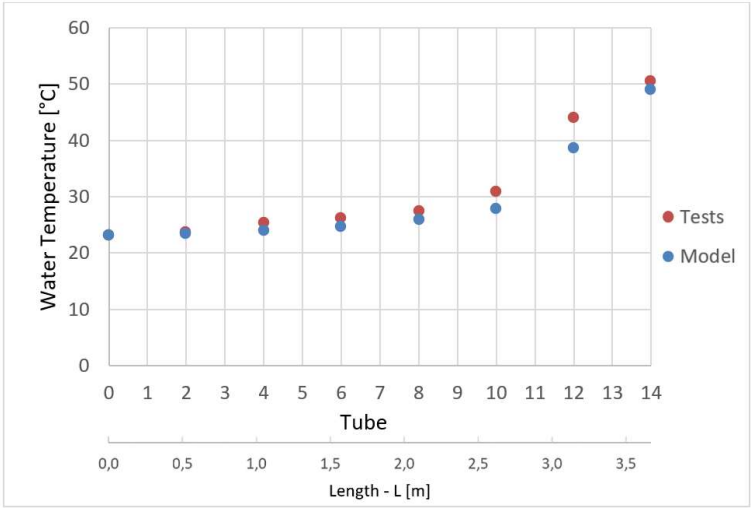

Figure 7.2. Water temperature results from the tests and model.

Even though this step might not have been enough to properly validate the models (due to all the constraints mentioned) it still served as a good indication, in the earlier stage when it was performed, that, overall, the simulations were producing solid and realistic results. These results, however, must now be compared to those obtained on the actual complete ORC installation in order to assure their validation, as will be done in the next section.

7.2. Final Validation

Once the ORC prototype's final installation had been completed, a series of tests were performed (as mentioned on Chapter 6). The parameters of each test which are relevant to the model's validation can be found in Annex C, Table C. 1.

Before comparing results, however, it is wise to mention that, due to the nature of the ORC prototype and the experimental component of this thesis work, it is only natural that the results are influenced by a series of measurement errors. Indeed, all the instruments used to measure the desired parameters have a certain degree of inaccuracy.

Taking this into account, Figure 7.3 shows the results for the Post-Heater (tests vs model) with the respective uncertainty interval. The two dots of each colour for each of the tested burner power (hard to distinguish on the model's results) represent the extremes of said interval. In this case, the variation on the absorbed power can be traced down to the temperature sensors no. 6.0 and 7 (Post-Heater's inlet and outlet, respectively) as well as the flowmeter - Table 6.3 (an average between the two flowmeters was used). These error calculations can be found in Annex D. These calculations were not performed for the evaporator due to the fact that the number of parameters which affect this component is much higher and their relations much more complex (fluid temperature, pressure, power absorbed on the post-heater and WF's flow rate – obtained indirectly).

Looking at Figure 7.3, it can be seen that the interval of values for the model's results is extremely small (so small that it's nearly impossible to see). This happens because the model only requires as input parameters two water flow characteristics (inlet temperature and mass flow rate) and performs the calculations according to these values. In the case of the tests, however, the value of ΔT_{water} is determined by two different sensors and, for a

fixed flow rate, a small variation in one of these temperatures may cause a significant change in the power absorbed.

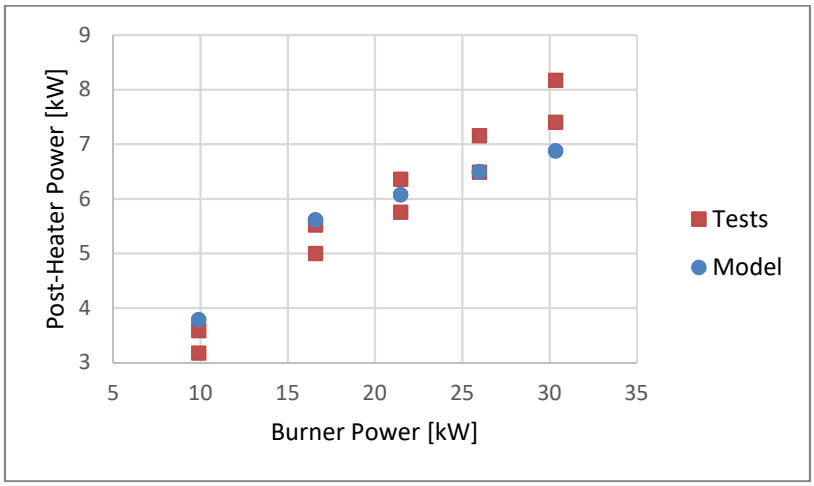

Figure 7.3. Power transferred in the Post-Heater for various levels of burner power.

Another conclusion which can be made is that, regardless of the sensor's inaccuracies, the results follow a clear trend – for the lowest power level, the model's results show a power transfer which is greater than the real value (by 11,2%, when comparing intervals' centres). This gradually changes as the power increases ending with a difference of -11,7% (in the opposite direction) for the maximum power test. This difference may obviously be lower due to measurement errors (since this error of -11,7% is the consequence of a small 2°C difference) but there is another phenomenon which is believed to cause this behaviour. Indeed, it is natural that, for the lowest power, the model calculates a higher ΔT_{water} since no thermal losses were accounted for. Even though the post-heater and evaporator section were thoroughly insulated, it was clear, during its operation, that losses did occur (especially on the post-heater as not only is the gas temperature in this section much greater but also there were two small glass "windows" built into the prototype in order enable visual contact with the flame). As the power is raised, however, small spots of steam begin to form along the post-heater's tubes. This was concluded not only due to the distinctive noise these steam areas generated during the tests but also due to the fact that the post-heater's model itself predicted an internal tube temperature above 100°C for all but the lowest power level.

The creation these areas of steam leads to a greater power absorption due to the increase of the internal convection coefficient. It is also clear that this phenomenon becomes

more relevant as the power is raised due to the higher temperatures reached (since it was not possible to raise the water's flow rate any further). By the time 30 kW are reached, the model predicts a lower power absorption on the post-heater than in reality as it does not account for such phenomenon. In the three remaining tests (performed at 16,7 kW) the error remained positive without ever exceeding 7%.

Now moving to the evaporator section, Figure 7.4 shows the evolution of the WF's temperature inside the evaporator for test no. 3 – burner power of 21,5 kW. This graph is representative of all the tests performed except no. 6 – two-phase flow (Figure 7.5).

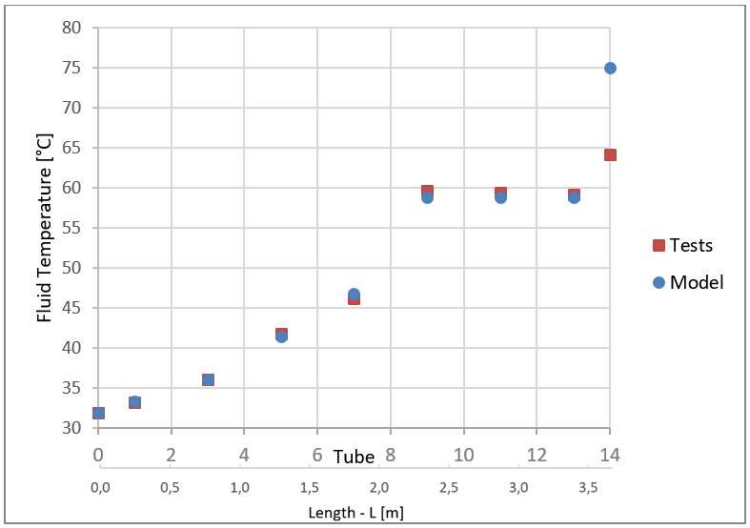

Figure 7.4. Fluid temperature in the Evaporator for a burner power of 21,5 kW.

As it can be seen, the WF's temperatures almost perfectly match except for the last value (where the fluid is superheated). However, despite the large temperature difference, the total power transfer "error" is only 5,5% (for this particular trial). Overall, the error is always positive (more power transferred in the model than in reality) starting from nearly 0 for the 1st test and rising until 10,3% for the 30,3 kW test (highest power). These translate into seemingly large temperature differences due to the fact that the fluid's c_p is relatively low, when in a gaseous state.

Once again, this difference may be explained by a few different phenomena (other than inaccuracies and limitations in the model itself). Firstly, it is important to notice that the thermocouple used to measure the fluid's outlet temperature was located not immediately after the evaporator but a reasonable distance further ahead, after a few

components that may induce some thermal losses which, as mentioned, may lead to large temperature variations. Nonetheless, this does not explain the growing trend in the error. In fact, the largest difference (percentwise) occurs for the maximum power which is where the maximum error in the post-heater is also verified. Additionally, these occur in opposite directions, that is to say, the model predicts a lower power transfer in the post-heater than in reality and a higher one in the evaporator. This may partially explain the difference. Indeed, if the post-heater were to transfer 1 extra kW (the difference for this test), it is likely that the evaporator would not transfer as much energy. It may not be enough to explain the 2 kW difference but it may be one of the causes. Finally, one must not forget how these results may also be affected by measurement errors which are probably even greater than on the post-heater due to the increased number of variables on which this process depends.

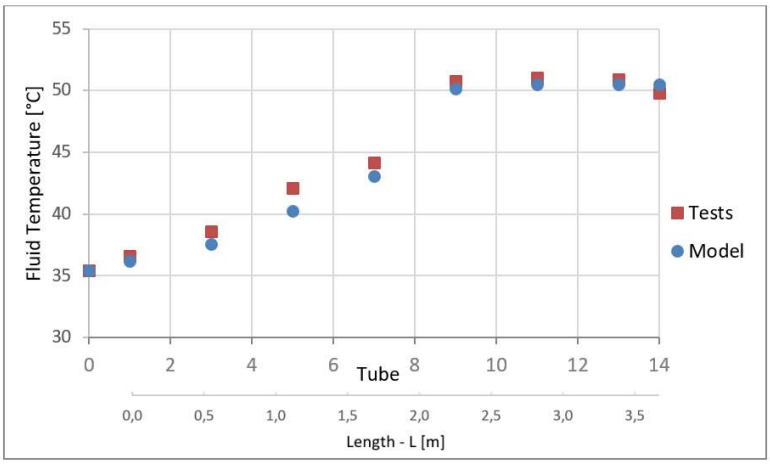

Figure 7.5. Fluid temperature in the Evaporator for a burner power of 16,7 kW.

As previously mentioned, Figure 7.4 is representative of all tests except for the one where the fluid was made to leave the evaporator in a two-phase flow instead of vapor. These results can be seen on Figure 7.5 and, although this graph cannot be supported by exact numbers (since the indirect way of calculating the fluid's flow rate does not allow the determination of the power transferred in this case) it shows that the temperatures match relatively well. In fact, in all tests, the two-phase region always matched perfectly (if small measurement errors are accounted for).

Finally, the evolution of the gas temperature as it travels through the Post-Heater and Evaporator is shown on Figure 7.6, for a burner power of 30,3 kW (test 5).

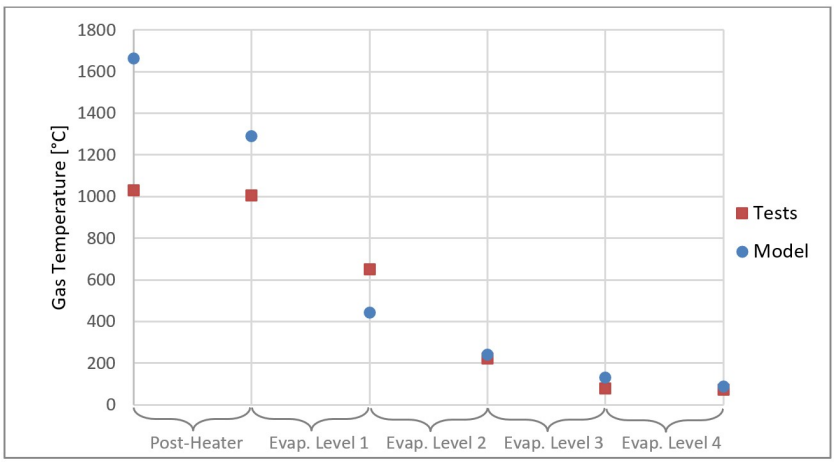

Figure 7.6. Gas temperature for a burner power of 30,3 kW.

Once again, the overall trend the temperature follows is similar for all tests. The largest difference is seen on the first point. The thermocouple type R placed in this location is supposed to measure the flame temperature but, as mentioned on section 7.1, it is subjected to large thermal losses including by radiation (this was confirmed when its probe was verified to be incandescent – visible through the "windows"). In addition, (and this is true for sensor 9 as well – located after the post-heater) this is the section where most of the thermal losses occurred due to high gas temperatures and weaker insulation. The remaining differences can be explained by other phenomena, namely the aforementioned power transfer difference between the model and the tests. Nonetheless, the exhaust temperature (sensor no.10) was very close for all 8 tests with some condensation often occurring.

In sum, despite not being perfect, in can be said that the model can predict the overall behaviour of the burner-post-heater-evaporator assembly, with the differences being justified by a series of physical phenomena not accounted for (losses, local evaporation, etc.) as well as measurement errors. It is also worth mentioning that the outputs shown were obtained without the use of any type of calibration factor which, as is known from experimental work, will most likely not lead to perfect results.

The following and final chapter of this dissertation will present the global conclusions to be made from this thesis in addition to making some remarks and recommendations for the future work to follow.

8. CONCLUSIONS

8.1. Global Conclusions

This thesis had, as a main goal, the development of a mathematical model capable of simulating the behaviour of a low power ORC evaporator, more precisely: a natural gas burner, a water post-heater and the working fluid evaporator. The model was developed on *Matlab* and divided in three parts - one for each component. Due to the lack of existing work on this specific area (small scale ORCs with direct evaporation and an incorporated post-heater), the adopted approach was that of starting with the more basic heat transfer phenomena along with some well-established correlations for compact heat exchangers.

Still during this development stage, the outputs the model was beginning to provide were compared to experimental results obtained in a preliminary test rig where water was used as a fluid. It was verified that (other than thermal losses which were particularly high during these tests) the simulation results described the behaviour of the evaporator satisfactorily well. This served as a preliminary validation for part of the model as the final ORC prototype was still being built at the time.

Simultaneously with the elaboration of the model, the construction of the final ORC prototype was taking place. This installation would use the organic fluid R245FA as a WF, cooled by water which would then travel through the post-heater (not present during the preliminary tests). This task proved itself as particularly challenging due to a number of reasons, one of which the novelty of such particular system.

Once the ORC prototype had been completed and was ready to operate, a series of tests were performed, subjecting the cycle to a variety of working conditions. Comparing these results to the model's outputs led to the conclusion that, although not being perfect (due to a number of phenomena not accounted for as well as possible limitations and inaccuracies in its construction), the model does describe the overall behaviour of this assembly of components. Being capable of simulating a series of intricate physical

phenomena with reasonable accuracy (taking into account the lack of calibration factors), the model proved to be useful. This usefulness comes from the possibility of knowing certain aspects of the behaviour of the evaporator which, for one reason or another, are particularly hard to measure/determine with experimental tests alone. Probably the most important of these is the hypothetical maximum temperature reached by the fluid during the ORC's operation. Although not calculated directly, the internal tube temperature does provide a good approximation to this parameter. Knowing this parameter is extremely useful to avoid/minimise the fluid's thermal degradation as well as to make recommendations for future work on this area.

In sum, it can be said that the main goal of this thesis work was achieved – the creation of a model capable of simulating this particular ORC evaporator with reasonable accuracy. This now leads to the final section of this dissertation – recommendations for future work.

8.2. Recommendations

During both the elaboration of the model and the construction of the ORC prototype, a series of challenges were faced and a number of key aspects discovered. Now, with both of them completed, it is possible to use the knowledge acquired during this process in order to improve and/or facilitate future work to be developed in this particular area. Starting by the model itself, there are a number of improvements that can be made (some of which could, however, be avoided with certain changes to the ORC prototype).

The first is related to the aforementioned WF maximum temperature. It was previously said, even though some results showed high values for this parameter, that those could be somewhat exaggerated as no conduction along the tube's walls was considered. Integrating this phenomenon in the model (if possible) could lower the maximum temperature in the inner wall by avoiding sudden "jumps".

The second recommendation concerns the post-heater and the occurrence of local evaporation of the water. Considering this possibility in the model could reduce/eliminate some of the discrepancies seen. Nonetheless, this could be avoided if some

changes were made to the installation such as the use of slightly pressurized water or the incorporation of some sort of turbulence generator inside the post-heater's tubes.

The third recommendation would be the modelling of heat transfer to the exterior of the evaporator (thermal losses). Given the complexity this would add to the model, better/more insulation could be used in the prototype instead.

Finally, although the two-phase region of the WF's flow appears to be well described by the model, the correlations used are mostly adequate for vertical and not horizontal tubes. It would be interesting to evaluate the heat transfer in this area with adequate correlations, if possible.

Concluding with the ORC prototype, it is recommended that more intrusive sensors are used for the high temperature/vapor sections as they proved to be more accurate than contact thermocouples in these parts of the installation. In addition, if new prototypes are built for this purpose, it would be advisable to use smaller or no fins in the first level in order to avoid the possibility of thermal degradation as lower temperatures would be reached with this change.

BIBLIOGRAPHY

[1] Ministério do Ambiente O do T e E. Decreto-Lei n.º 68-A/2015. Portugal: Diário da República n.º 84/2015, 1º Suplemento, Série I de 2015-04-30; 2015.

[2] Pereira JS, Ribeiro JB, Mendes R, Vaz GC, André JC. ORC based micro-cogeneration systems for residential application - A state of the art review and current challenges. Renew Sustain Energy Rev 2018. doi:10.1016/j.rser.2018.04.039.

[3] Pereira JS, Ribeiro JB, Mendes R, Vaz GC, André JC. Development of a direct concept helical-coil evaporator for an ORC based micro-CHP system. Energy Procedia 2017;129:474–8. doi:10.1016/j.egypro.2017.09.162.

[4] Angelino G, Invernizzi C. Experimental investigation on the thermal stability of some new zero ODP refrigerants. Test 2003;26:51–8.

[5] Pereira JS, Ribeiro JB, Mendes R, André JC. Analysis of a hybrid (topping/bottoming) ORC based CHP configuration integrating a new evaporator design concept for residential applications. Appl Therm Eng 2019. doi:10.1016/j.applthermaleng.2019.113984.

[6] Liuchen LIU, Tong ZHU, Naiping GAO, Zhongxue GAN. A review of modeling approaches and tools for the off-design simulation of organic Rankine cycle. J Therm Sci 2018;27:305–20. doi:10.1007/s11630-018-1023-2.

[7] Jiménez-Arreola M, Pili R, Wieland C, Romagnoli A. Analysis and comparison of dynamic behavior of heat exchangers for direct evaporation in ORC waste heat recovery applications from fluctuating sources. Appl Energy 2018;216:724–40. doi:10.1016/j.apenergy.2018.01.085.

[8] Jiménez-Arreola M, Wieland C, Romagnoli A. Direct vs indirect evaporation in Organic Rankine Cycle (ORC) systems: A comparison of the dynamic behavior for waste heat recovery of engine exhaust. Appl Energy 2019;242:439–52. doi:10.1016/j.apenergy.2019.03.011.

[9] Mills AF. Heat and Mass Transfer. 1st ed. Los Angeles: Richard D. Irwin Inc.;

1995.

[10] Incropera FP, DeWitt DP, Bergman TL, Lavine AS. Fundamentals of Heat and Mass Transfer 6th Edition. 2007. doi:10.1016/j.applthermaleng.2011.03.022.

[11] André JC, Ribeiro JB, Costa E, Santos M, Francisco S. Relatório T3.4-2. Coimbra: 2013.

[12] FinTube. FINBRAZE® Brazed Finned Tubing 2019. http://www.fintube.com/finbraze-tubing.html (accessed July 15, 2019).

[13] Neutrium. Pressure Loss from Fittings – Excess Head (K) Method – Neutrium 2012. https://neutrium.net/fluid_flow/pressure-loss-from-fittings-excess-head-k-method/ (accessed July 5, 2019).

[14] ThermExcel. Local pressure loss 2019. https://www.thermexcel.com/english/ressourc/pdclocal.htm (accessed July 5, 2019).

[15] R. Byron Bird Warren E. Stewart Edwin N. Lightfoo, Bird RB, Stewart WE, Lightfoot EN. Transport Phenomena, Revised 2nd Edition. 2006. doi:10.1002/aic.690070245.

[16] Chemistry LibreTexts. Propagation of Error 2019. https://chem.libretexts.org/Bookshelves/Analytical_Chemistry/Supplemental_Modules_(Analytical_Chemistry)/Quantifying_Nature/Significant_Digits/Propagation_of_Error (accessed August 30, 2019).

ANNEX A

Transport Properties of a Gas Mixture

The method adopted to calculate the dynamic viscosity and thermal conductivity of the combustion gases is presented by Bird *et al.* [15] on the "*Viscosity and the Mechanisms of Momentum Transport*" section. Now, the dynamic viscosity of the mixture is calculated using the *semi-empirical formula of Wilke* (A. 1):

$$\mu_{mix} = \sum_{i=1}^{n} \frac{y_i * \mu_i}{\sum_{j=1}^{n} y_i * \varphi_{ij}} \quad \text{(A. 1)}$$

With:

$$\varphi_{ij} = \frac{1}{\sqrt{8}}\left(1 + \frac{M_i}{M_j}\right)^{-\frac{1}{2}} [1 + \left(\frac{\mu_i}{\mu_j}\right)^{\frac{1}{2}} \left(\frac{M_j}{M_i}\right)^{\frac{1}{4}}]^2 \quad \text{(A. 2)}$$

Where: n = 4 (4 substances which make the combustion gases); y_i is the molar fraction of the compound *i*; μ_i [Pa.s] is the dynamic viscosity of the compound *i*; M_i [kg/mol] is the molar mass of the compound *i*.

In a similar fashion, the mixture's thermal conductivity is obtained the following way ("*Thermal Conductivity and the Mechanisms of Energy Transport*", [15]), eq. (A. 3):

$$k_{mix} = \sum_{i=1}^{n} \frac{y_i * k_i}{\sum_{j=1}^{n} y_i * \varphi_{ij}} \quad \text{(A. 3)}$$

Where k [W/m.K] is the thermal conductivity of each individual compound.

Once these two properties have been obtained, the *Prandtl* number can be calculated by equation (A. 4):

$$Pr_g = \frac{cp_{film,g} * \mu_g}{k_g} \quad \text{(A. 4)}$$

Where: $cp_{film,g}$ [J/kg.K] is the gases' cp, evaluated at film temperature; k_g [W/m.K] is the gases' thermal conductivity.

In order to assess the difference between following this method or simply calculating these properties using mass and molar weighted averages, Table A. 1 and Table A. 2 (where the three different results are compared) were constructed. It can be observed that the effect this has on the convective heat transfer coefficient is significant if the gas temperature is relatively low. Since low exhaust temperatures are expected to be reached, this approach was maintained even if more complex.

Table A. 1. Effect of different methods for calculating gas properties on *h* (for T_film = 731 K)

Tg_ft = 731 K						
	h $[W/m^2.K]$	Error [%]	μ [Pa/s]	Error [%]	K [W/m.K]	Error [%]
Chosen Method	35,139	-	3,337E-05	-	0,054	-
Mass fraction	34,846	**-0,836**	3,352E-05	**0,456**	0,053	**-1,117**
Molar Fraction	35,163	**0,067**	3,315E-05	**-0,650**	0,054	**-0,186**

Table A. 2 Effect of different methods for calculating gas properties on *h* (for T_film = 325 K)

Tg_ft = 325 K						
	h $[W/m^2.K]$	Error [%]	μ[Pa/s]	Error [%]	K [W/m.K]	Error [%]
Chosen Method	31,611	-	2,443E-05	-	0,033	-
Mass fraction	43,439	**37,415**	6,559E-05	**168,436**	0,083	**150,150**
Molar Fraction	48,625	**53,822**	9,174E-05	**275,484**	0,115	**244,144**

ANNEX B

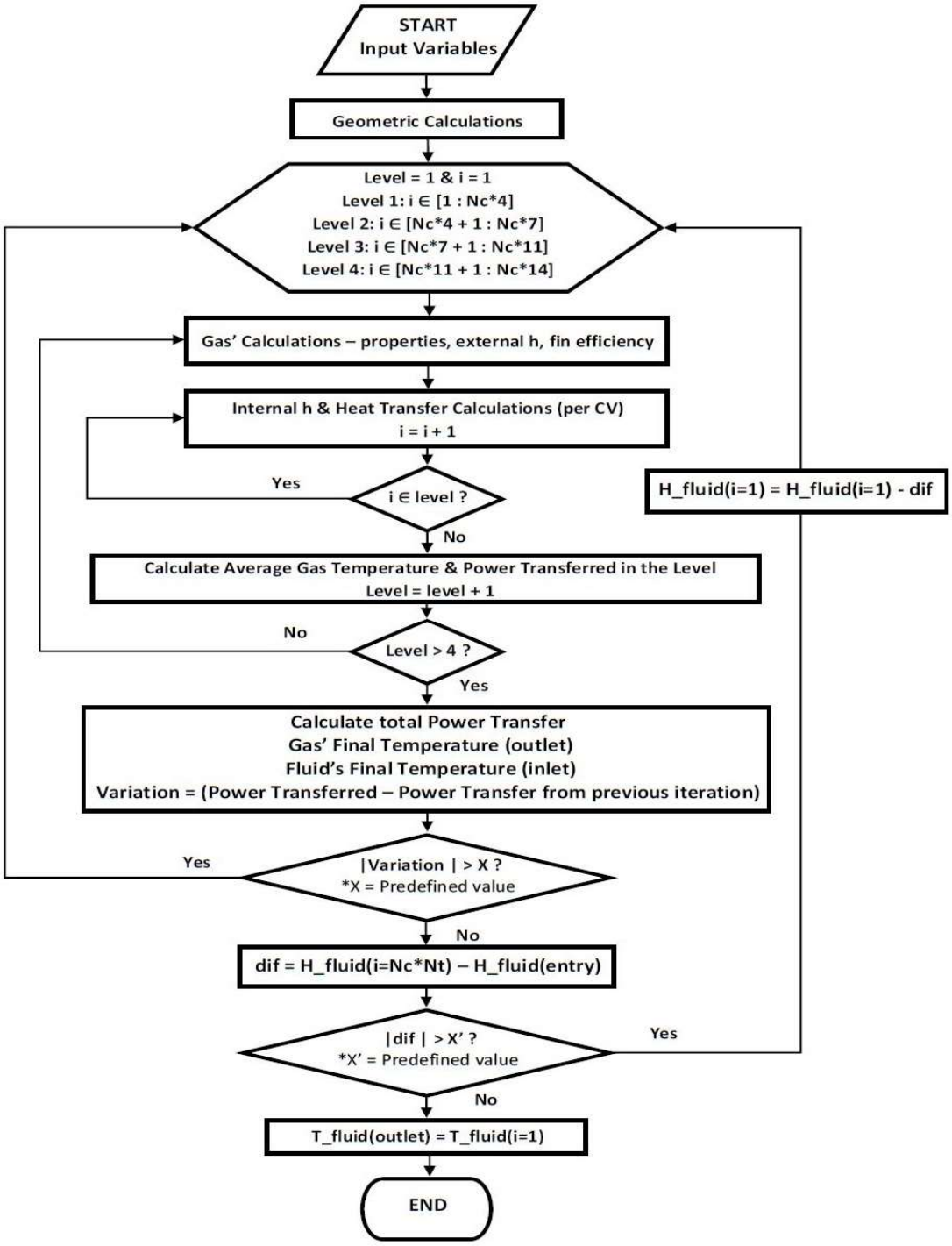

Figure B. 1. Flow-chart of the evaporator model. The iterative process controlled by the variable *variation* also applies to the one used on the post-heater model, where the control variable is named *error*.

ANNEX C

Table C. 1. Experimental tests parameters.

Test	C_{NG} $[m^3/300s]$	P_{burner}. [kW]	$\dot{m}_{water}$ [kg/s]	T 6 [°C]	T 6.5 [°C]	T 7 [°C]
1	0,077	9,883	0,1082	36,4	40,6	44,0
2	0,129	16,583	0,1088	43,8	50,1	55,5
3	0,167	21,465	0,1075	51,1	58,7	64,7
4	0,202	25,963	0,1064	57,4	66,2	73,0
5	0,236	30,334	0,1178	59,5	68,6	75,6
6	0,13	16,704	0,1088	44,8	51,2	55,9
7	0,13	16,704	0,1129	43,6	49,8	54,5
8	0,13	16,704	0,0694	55,1	65,0	72,1

Test	$\dot{m}_{fluid}$ [kg/s]	Pf [bar(g)]	T 1 [°C]	T 1.1 [°C]	T 1.2 [°C]	T 1.3 [°C]	T 1.4 [°C]	T 1.5 [°C]	T 1.6 [°C]	T 1.7 [°C]	T 2 [°C]
1	0,0257	1,70	25,5	27,3	30,0	36,3	39,0	42,5	42,9	42,8	46,7
2	0,0428	2,55	28,1	29,4	32,9	38,4	42,1	51,9	51,5	51,6	55,1
3	0,0583	3,47	31,9	33,1	36,1	41,7	46,2	59,6	59,3	59,2	64,1
4	0,0702	4,53	34,0	35,3	38,2	45,8	53,7	68,6	67,0	66,7	71,1
5	0,0833	5,03	35,0	36,4	39,4	48,0	57,6	70,9	70,3	70,1	74,8
6	0,0660	2,49	35,4	36,6	38,6	42,1	44,2	50,8	51,0	50,9	49,8
7	0,0432	2,68	27,6	28,6	32,2	39,0	42,9	53,2	52,8	52,8	62,1
8	0,0430	3,59	32,6	33,9	36,8	42,6	46,5	61,6	60,3	60,4	65,2

Test	T 8 [°C]	T 9 [°C]	T 9.1 [°C]	T 9.2 [°C]	T 9.4 [°C]	T 10 [°C]	%O2	Exc. Air [%]
1	843	791	414	55	47	47	8,0	55,4
2	986	938	600	77	55	57	4,8	26,7
3	995	960	635	89	62	63	5,1	28,9
4	1009	980	635	202	74	68	5,1	28,9
5	1031	1006	651	221	80	73	5,1	28,9
6	951	908	611	73	55	57	5,9	35,2
7	951	914	629	79	56	58	5,9	35,2
8	951	916	635	85	61	61	5,9	35.2

ANNEX D

Experimental Uncertainty Calculation

The power transferred in the post-heater during the tests was determined using equation (D. 1), where ΔH_{water} is calculated using the inlet and outlet temperatures (T_{in} and T_{out}, respectively). However, in order to allow for an analytical error calculation, it will be now replaced by eq. (D. 2) with *cp* being measured at a mean temperature.

$$Q_{water} = \dot{m}_{water} * \Delta H_{water} \quad \text{(D. 1)}$$

$$Q_{water} = \dot{m}_{water} * cp_{water} * \Delta T_{water} = \dot{m}_{water} * cp_{water} * (T_{out} - T_{in}) \quad \text{(D. 2)}$$

It is known that the standard deviation of a function *x* (σ_x) can be given by the equation (D. 3), when $x = a + b$ and eq. (D. 4), when $x = a*b$ with *a* and *b* being two variables with a given uncertainty (see [16]).

$$\sigma_x = \sqrt{{\sigma_a}^2 + {\sigma_b}^2} \quad \text{(D. 3)}$$

$$\sigma_x = x * \sqrt{(\frac{\sigma_a}{a})^2 + (\frac{\sigma_b}{a})^2} \quad \text{(D. 4)}$$

Therefore, calculating the uncertainty of Q_{water} can be done in two steps:

- In the first one, the considered function is $cp_{water} * \Delta T_{water}$. Being cp_{water} a constant, the resulting σ is given by equation (D. 5).

$$\sigma_{cp_{water}*\Delta T_{water}} = cp_{water} * \sqrt{{\sigma_{T\ out}}^2 + {\sigma_{T\ in}}^2} \quad \text{(D. 5)}$$

- The second step considers the multiplication of the previous function by $\dot{m}_{water}$, which leads to equation (D. 6).

$$\sigma_{Q_{water}} = Q_{water} * \sqrt{\left(\frac{\sigma_{cp_{water}*\Delta T_{water}}}{cp_{water} * \Delta T_{water}}\right)^2 + \left(\frac{\sigma_{\dot{m}_{water}}}{\dot{m}_{water}}\right)^2} \quad \text{(D. 6)}$$

The interval is obtained by adding and subtracting $\sigma_{Q_{water}}$ to the determined value of the power transferred. $\sigma_{T\ out}$, $\sigma_{T\ in}$ and $\sigma_{\dot{m}_{water}}$ are calculated using equation (D. 7).

$$\sigma_v = v * error_{sensor} \quad \text{(D. 7)}$$

Where v is the variable and $error_{sensor}$ is the maximum error in each sensor, displayed on Table 6.1 and Table 6.3.

Since the maximum error of Q_{water} calculated by the model cannot be obtained analytically, the interval was determined by running the simulation with the input parameters (temperature and flow rate) at their minimum and maximum. This provides the results for the two extreme cases, enabling the creation of said interval.

These calculations were performed for each of the tests shown in Figure 7.3.

ANNEX E

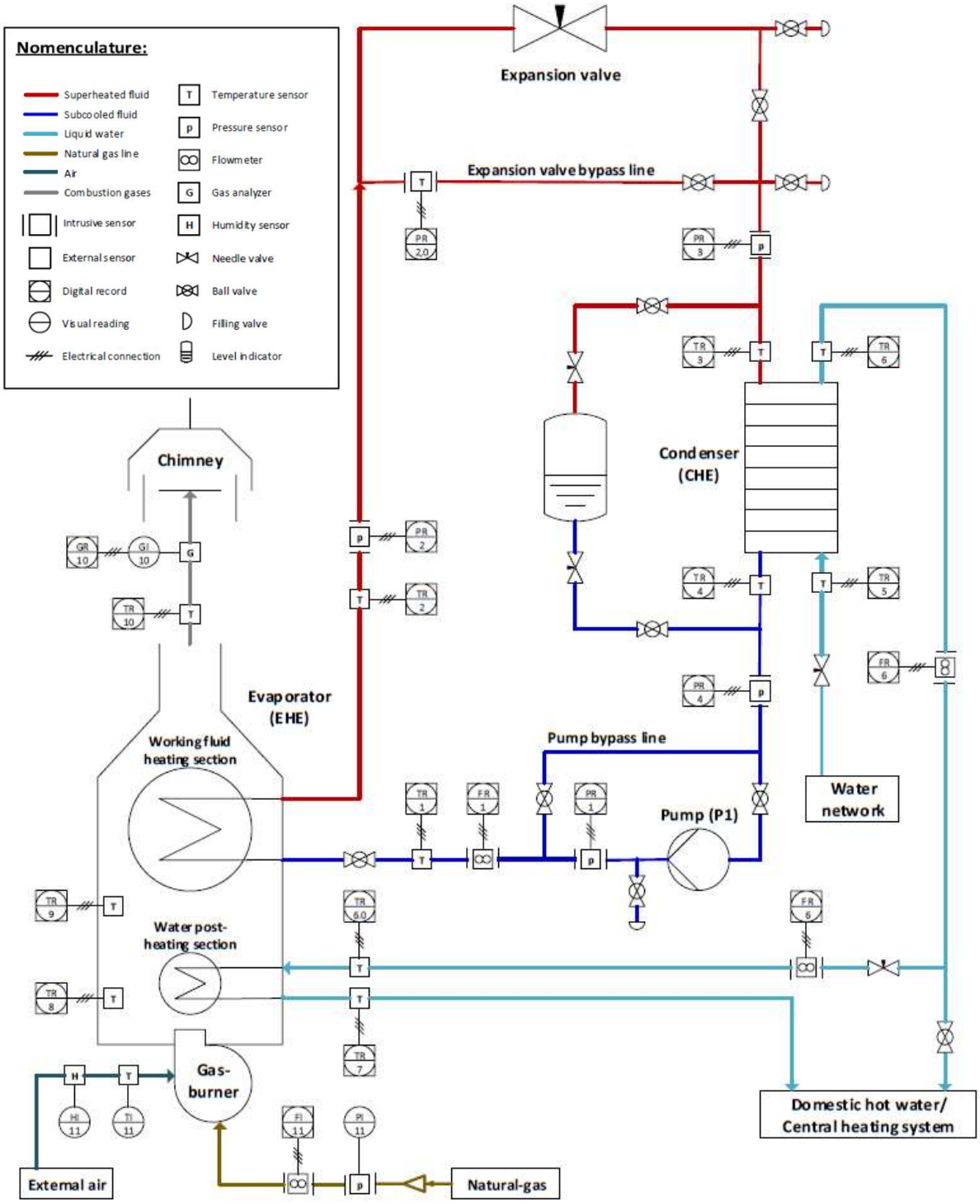

Figure E. 1 Working diagram of the complete ORC prototype.